

QUANTUM PHASE COHERENCE AND CORRELATION EFFECTS IN A
STRAINED SrTiO₃ FILM EPITAXIALLY GROWN ON P-Si (100)

by

Barry Dean Koehne, B.S.

A thesis submitted to the Graduate Council
of Texas State University in partial fulfillment
of the requirements for the degree of
Master of Science
with a Major in Physics
August 2019

Committee Members:

Nikoleta Theodoropoulou, Chair

Ethan Ahn

Wilhelmus Geerts

COPYRIGHT

By

Barry Dean Koehne

2019

FAIR USE AND AUTHOR'S PERMISSION STATEMENT

Fair Use

This work is protected by the Copyright Laws of the United States (Public Law 94-553, section 107). Consistent with fair use as defined in the Copyright Laws, brief quotations from this material are allowed with proper acknowledgement. Use of this material for financial gain without the author's express written permission is not allowed.

Duplication Permission

As the copyright holder of this work I, Barry Dean Koehne, authorize duplication of this work, in whole or in part for educational or scholarly purposes only.

ACKNOWLEDGEMENTS

Thank you to Dr. T and to John for all the help that you have given me with out you this could not have been completed. Thank you to everyone in our research

TABLE OF CONTENTS

	Page
ACKNOWLEDGEMENTS	iv
LIST OF TABLES	vii
LIST OF FIGURES	viii
LIST OF ABBREVIATIONS.....	xii
CHAPTER	
1. INTRODUCTION	1
1.1 SrTiO ₃ (bulk properties)	1
1.2 SrTiO ₃ (2d properties).....	2
1.3 SrTiO ₃ on Si.....	4
1.4 Motivation.....	6
1.5 Introduction to 2d transport	7
2. METHODOLOGY: GEOMETRY AND SETUP	12
2.1 Van der Pauw geometry.....	12
2.2 Electronics.....	15
2.3 Hall bar measurement setup.....	18
3. GROWTH AND CHARACTERIZATION OF SrTiO ₃ FILMS ON Si.....	19
4. NANOFABRICATION OF HALL BAR	23
4.1 Process overview	23
4.2 Ion Milling	28
4.3 AFM-Hall Bars	30
4.4 Deposition	31
4.5 SEM	32
4.6 Contact metal evaluation.....	34

5. TRANSPORT ANALYSIS OF SrTiO ₃ /Si Van der Pauw.....	35
5.1 Temperature dependence of R _s	35
5.2 Magnetoresistance.....	40
5.2.1 MC fitting using the HLN expression with two parameters	42
5.2.2 MC fitting using the HLN expression with one parameter.....	46
5.3 3-D kinematic data.....	48
5.4 Hall Resistance.....	50
5.5 Parabolic HLN Fitting.....	53
6 CONCLUSIONS.....	56
6.1 Conclusion	56
6.2 Hall bar data	59
6.3 Future directions	63
APENDIX SECTION	64
REFERENCES	65

LIST OF TABLES

Table	Page
1. List of equations used in paper	10
2. Sample growth parameters	22
3. Ion milling parameters	29
4. Sample carrier concentrations.....	52
5. Sample substrates	57

LIST OF FIGURES

Figures	Page
1. Lifshitz point	3
2. STO lattice orientation	4
3. Energy band diagram	5
4. Van der Pauw geometry	12
5. Van der Pauw contacts	13
6. PPMS probe	15
7. Keithley 7065 hall effect card schematic	15
8. Van der Pauw schematics	16
9. Van der Pauw channels	16
10. Hall channels	17
11. Hall schematics	18
12. SEM images	19
13. AFM scan	20
14. Phi scan	20

15. XRD scans	21
16. Photoresist Spin Speed Curve	24
17. Dose to Clear (DTC).....	25
18. Ion Miller.....	28
19. AFM scan of sample B hall	30
20. SEM images of Cr contacts on STO.....	32
21. Hall bar dimensions	33
22. Sheet resistance	35
23. lnT dependence	36
24. Minimizing QCC	37
25. Estimated σ_D	37
26. ES-VRH	38
27. 2D-VRH	38
28. 3D-VRH	39
29. Magneto resistance	40
30. 2 K MR	41

31. Magneto conductance	41
32. HLN2	42
33. 2K HLN2.....	43
34. 2K MC HLN2	43
35. B_{tr}	44
36. τ_{calc} and τ_{fit}	45
37. HLN1	46
38. 2K MC HLN1	47
39. 3D fit.....	48
40. R_{xy}	50
41. Electron Electron Interaction	50
42. 2K hall slope	51
43. Hall slope.....	51
44. Carrier concentration vs $\ln T$	52
45. HLN3	54
46. 2K MC HLN3	54

47. D HLN3.....	55
48. HLN 1,2,3.....	55
49. Characteristic Lengths	56
50. Cr contacts.....	59
51. Different contacts.....	60
52. MR.....	61
53. Rxy of AC	61

LIST OF ABBREVIATIONS

Abbreviation	Description
2DEG - two-dimensional electron gas	
2D - two-dimensional	
Å – Angstroms	
ACT – AC Transport	
Al - Aluminum	
Au - Gold	
AFM - Atomic-force Microscopy	
C - Celsius	
DI water - deionized water	
DTC - Dose to Clear	
EEI – Electron Electron Interaction	
GaAs - Gallium Arsenide	
GaAlAs - Gallium Aluminum Arsenide	
He - Helium	
IPA - Isopropyl Alcohol	
K - Kelvin	
LAO - LaAlO ₃	
MBE - Molecular Beam Epitaxy	
NMP - N-Methyl-2-pyrrolidone	
NRSS - Nanofabrication Research Shared Space	
PPMS - Physical Property Measurement System	
QCC - Quantum Correction to Conductivity	
RPM - Revolutions Per Minute	

SEM - Scanning Electron Microscope

Si - Silicon

SiO₂ - Silicon Dioxide

SOC - Spin Orbit Coupling

STO - SrTiO₃

XRD - X-ray Diffraction

WL - Weak localization

WAL - Weak antilocalization

Electron charge	$e = 1.60217 \times 10^{-19} C$
Electron mass	$m_e = 9.109 \times 10^{-31} kg$
Quantum conductance	$G_0 = \frac{e^2}{\pi h} = 1.23 \times 10^{-5} S$
Quantum resistance	$R_0 = \frac{h}{e^2} \cong 25.8 k\Omega$
Planck's constant	$h = 6.626 \times 10^{-34} J * s$
Dirac constant	$\hbar = \frac{h}{2\pi} = 1.054 \times 10^{-34} J * s$

1. INTRODUCTION

1.1 SrTiO₃ (bulk properties)

ABO₃-type perovskite crystals are important for numerous technological applications in electro-optics, waveguides, laser frequency doubling, high capacity computer memory cells, etc¹. SrTiO₃ like other perovskites has a simple cubic structure; in this structure oxygen atoms, located in the face-center positions of a cubic unit cell, form a perfect octahedron with the titanium atom in its center, and strontium, barium or lead atoms lying outside the oxygen octahedron, in corners of a cube. The bulk STO band gaps are 3.25 eV (indirect gap) and 3.75 eV (direct gap)¹. Undoped STO is a band insulator but can be doped n-type or p-type by substitution of different elements or by creating Oxygen vacancies which generates two free electrons per vacancies.²

1.2 SrTiO₃ (2d properties)

The coupling of the electrons' charge and spin to the lattice and to each other determine the physical properties of this 2D system and can be determined and perhaps controlled by strain ³, chemical doping ⁴ or atomic composition ⁵, conduction and valence band offsets at the interface ⁶. In a two-dimensional electron gas (2DEG), a confining potential well of less than 50 nm will quantize the electronic motion in the direction of the potential variation, while allowing the carriers to move freely in the other two dimensions. The dimensionality of a system relates to its density of states. The de Broglie wavelength of the carriers must be long enough to be comparable to the sample dimensions. In general, a quantum well is not necessary to obtain 2D electrons. An epitaxial, abrupt interface between two different materials plus an electric field of ionized donors gives the same effect. The 2D electron system at the surface of SrTiO₃⁷, at the interface between SrTiO₃ and oxides ⁸, and in δ-doped SrTiO₃⁴ has been investigated intensely in the past decade. Figure 1 illustrates the different energy orbitals in momentum space of a LAO/STO system. The Lifshitz point indicated in Figure 1 occurs when the Fermi energy exceeds a critical value at which point different bands can be occupied at the same time. Below a critical carrier density all electrons are expected to reside in the d_{XY} band and only one type of carrier exists in the system. At higher

densities the Fermi energy enters the d_{xz} and d_{yz} bands, and as they both get populated, we expect to observe contributions from multiple carrier type.⁹

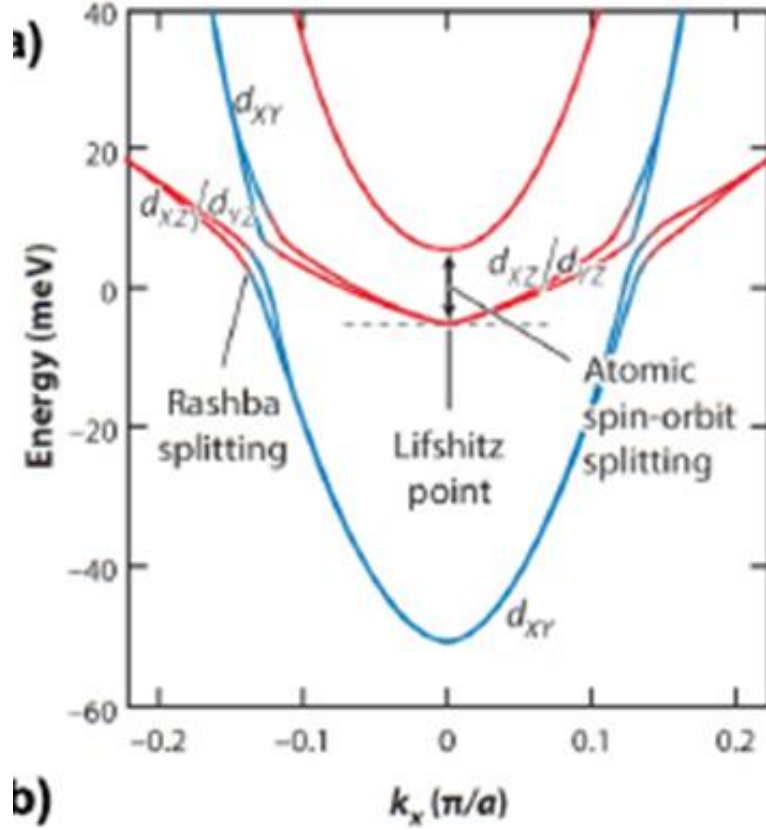


Figure 1. Lifshitz point. Fermi energy in momentum space indicating a Lifshitz point where multiple band filling of energy state can occur.

1.3 SrTiO₃ on Si

STO forms a cubic lattice at room temperature with a lattice constant of $a = 3.905 \text{ \AA}$ whereas Si has a lattice constant of $a = 5.431 \text{ \AA}$. STO grows pseudo

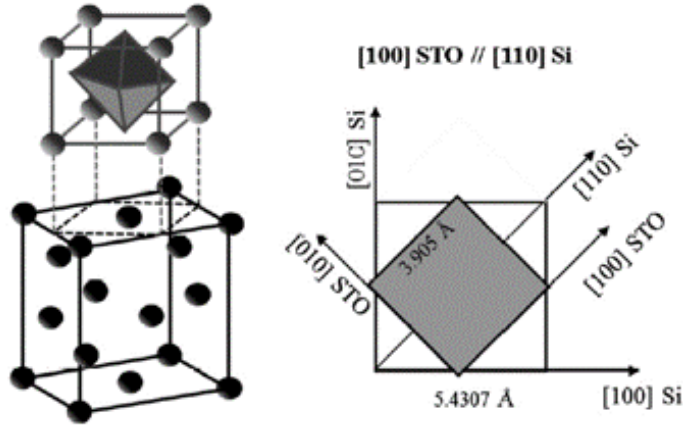


Figure 2. STO lattice orientation. STO has a 45-degree rotation to match up to the Si

morphically on Si(100) by a 45° rotation around the surface normal, STO[100]||Si[110] as seen in figure 2.¹⁰ A coherent growth produces a compressive in-plane strain of 1.7% and a tetragonal distortion with a c/a ration of 2.7%.^{11 12} As the thickness increases, the lattice relaxes with a critical thickness of ~9 nm for high P_{O_2} and ~14 nm for low P_{O_2} .¹³

¹¹ The conduction and valence band offsets (CBO,VBO) of the heterojunction have been calculated¹⁴ and measured by XPS and UPS *in-situ*¹⁵ and *ex-situ*^{16, 17}. The STO conduction band is reported to be below the Si conduction band with reported CBO values varying from 0.4eV¹⁸ to 0 eV. The experimentally determined CBO values depend on the precise growth procedure, the interface chemistry, the STO surface treatment, and the substrate type n-Si vs p-Si.^{15 16, 18} The strain-induced tetragonal distortion in SrTiO₃/Si induces a large polarization and leads to splitting of the degenerate t_{2g} levels with the d_{xy} band edge lower in energy than the elliptical d_{zx} and d_{yz} bands¹⁹. The

SrTiO₃/Si CBO, the SrTiO₃ surface band bending⁷ and a strain-induced polarization²⁰

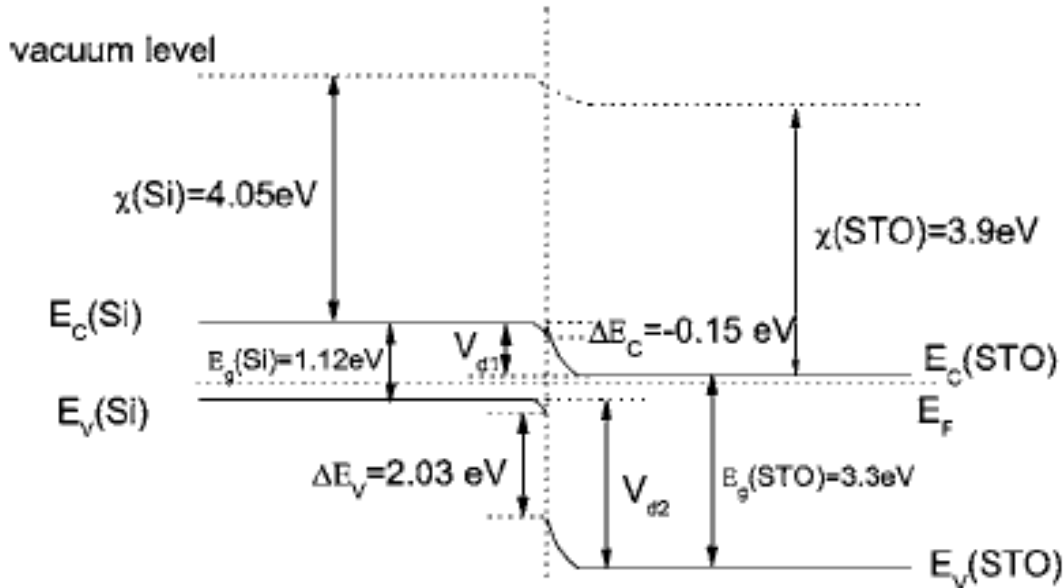


Figure 3. Energy band diagram. The energy band diagram of the STO/Si junction.

could contribute to an electrostatic potential providing complete quantum confinement for some of the energy bands.²¹ If the dimensions of a crystalline solid are reduced to the size of the wavelength of electrons, the formerly continuous energy bands split into discrete energy levels.²² The CBO of the STO/Si interface can act as a potential well with a one-dimensional confinement.

1.4 Motivation

The growth of epitaxial STO on p-type Si (001) have been studied extensively over the last 20 years however very limited research has been conducted correlating the growth to transport behavior. Preliminary transport measurements conduced at temperatures below 30K by our group showed characteristic behavior of a 2D electron system. Specifically, we observed 2D Weak Localization, a $\ln T$ dependence of the conductivity and negative magneto resistance. The Hall measurements of the system shows the charge carriers to be electrons which are most likely contributed by the STO film, as oxygen deficient STO is n-type. To test that the substrate does not affect this electronic transport behavior we investigate the transport of STO films with similar growth conditions on p Si substrates with different doping level.

1.5 Introduction to 2d transport

The resistance of different types of materials (semiconductor, metal, ...etc.) has different behavior as the temperature is changed. The resistance of semiconductor materials increases as the temperature is lowered. The Boltzmann transport theory predicts that at low temperatures the conductivity of disordered conductors is limited by the elastic scattering of electrons from disorder (impurities, lattice defects). The low-temperature transport behavior in 2D systems is determined by quantum effects to the conductance when disorder is high. The quantum corrections to the Drude conductivity are divided into two groups according to the physical mechanism. The first type of corrections is caused by quantum interference of electrons that are coherently backscattered by impurities, the Weak Localization (WL) corrections. The second type of corrections is due to inelastic scattering of electrons by other electrons, the Electron-electron interaction (EEI).²³ In 2D, in the diffusive regime where $\frac{k_B T \tau}{\hbar} < 1$, $\tau_\phi \gg \tau$ both quantum corrections are logarithmic in T ^{24 25, 26}, $\delta\sigma_{WL}(T) = G_0 \ln[\frac{\tau}{\tau_\phi(T)}]$ is always negative and $\delta\sigma_{EEI}(T) = G_0 K_{ee} \ln \frac{k_B T \tau}{\hbar}$ can be positive or negative²⁴ depending on the value of $K_{ee} = 1 + 3 \left(1 - \frac{\ln(1+F_0^\sigma)}{F_0^\sigma}\right)$ where F_0^σ is the Fermi-liquid constant determined by spin-exchange interactions. The diffusion theory of WL works down to $\frac{k_B T \tau}{\hbar} \ll 1$ and is quite often used to analyze results for more disordered quantum well systems.²⁷ Since WL leads to an enhancement of the resistance due to the constructive interference of closed electron trajectories which are “traveled” in the opposite direction (time-reversed paths), applying a magnetic field B destroys the constructive interference, leading to a negative

magnetoresistance $R_s(B)$ whose amplitude and width is directly related to the phase coherence time. The shape of the low-field negative magnetoconductance caused by suppressing the interference correction is described by the Hikami-Larkin-Nagaoka (HLN) expression²⁸ found in table 1. The HLN expression uses ψ the digamma function, B_ϕ the phase coherence field, and B_{tr} the transport field to describe how the MC acts in a magnetic field. The temperature and field dependence of WL is determined by a time, τ_ϕ , the dephasing (inelastic scattering) time representing the coherence duration of the electronic wave function. It relates to the corresponding length scale, the diffusion length by the Diffusion constant, D . The dephasing time in 2D semiconductor systems at low temperatures is determined by the inelasticity of the Coulomb electron-electron interaction²⁹. The second type of correction EEI does not contribute to the MC (longitudinal resistivity)³⁰ unless the Zeeman energy is comparable to the thermal energy, $b = g\mu_B B/k_B T \gtrsim 1$, where g is the gyromagnetic ratio of electrons and μ_B is the Bohr magneton. It is also predicted that WL does not affect the Hall resistance, R_H while EEI obey: $\frac{(\delta R_H)_{EEI}}{R_H} = -2 \frac{(\delta \sigma_d)_{EEI}}{\sigma_d}$ as $T \rightarrow 0$.³¹ The absolute value of both interference and interaction corrections increases with decreasing Temperature. Also as disorder increases, τ decreases, the absolute value of the corrections also increases leading to a strong Temperature dependence of the conductivity that we also observe and the conductivity corrections become comparable to the Drude conductivity.³² The phase coherence length l_ϕ and thermal length $l_T = \sqrt{\hbar D/k_B T}$ set the dimensionality for interference and interaction effects respectively²³. In a 3D system conduction is primarily by carriers in delocalized states, but in a 2D system the carriers can be localized if disorder is strong or EEI dominate which gives rise to Variable-Range Hopping (VRH). It immediately

follows that with increasing disorder (decreasing τ) or decreasing temperature both corrections get enhanced in magnitude and can become comparable to Drude conductivity³³ leading to a transition from logarithmic conductivity to hopping conductivity³⁴. In the variable-range hopping (VRH) regime, $R_s = R_o e^{(T_o/T)^p}$ where $R_s = 1/\sigma$ is the sheet resistance, $p = 1$ for nearest-neighbor hopping (thermally activated), $p = \frac{1}{d+1}$ for non-interacting, d-dimensional systems when VRH is caused by disorder, and $p = 1/2$ when Coulomb interactions between electrons are included (Efros-Shklovskii-ES-VRH), R_o and T_o are sample-characteristic parameters.³⁵ If the system is not in a 2 DEG state then the RvT will not have a lnT dependence and the field dependence will have to be evaluated with the sample thickness. The sheet concentration will need to be a volume concentration and it will have to be evaluated not only as the sample thickness but also as the possibility that the effective thickness will be a small portion of the sample thickness while still being in a 3D state. The resistance temperature dependence of a 3D semiconductor device is $T^{\frac{3}{2}}$.³⁶ All results that are reported in this paper come from the measured resistance as a function of temperature and magnetic field. The equations used to support the later analyses can be found in Table 1 below.

Table 1. List of equations used in paper

Eq 1	Drude Conductance	$\sigma_D = en_s\mu = \frac{e^2 n_s \tau}{m^*} = \pi G_0 k_F l$
Eq 2	Sheet Carrier concentration B magnetic field, e electron charge	$n_s = \frac{B}{eR_{xy}}$
Eq 3	Volume Carrier concentration d thickness	$n_v = \frac{n_s}{d}$
Eq 4	Effective mass of electron	$m^* = 1.2m_e$
Eq 5	Diffusion constant	$D = \frac{\pi \hbar^2 \sigma_D}{e^2 m^*}$ $D = \frac{1}{2} l^2 \tau$
Eq 6	Phase coherence field	$B_\phi = \frac{\hbar}{4eD\tau_\phi} = \frac{\hbar}{4el_\phi^2}$
Eq 7	Transport field	$B_{tr} = \frac{\hbar}{2eD\tau} = \frac{\hbar}{2el^2}$
Eq 8	Fermi velocity	$v_F = \frac{\hbar k_F}{m^*}$
Eq 9	Scattering time	2D $\tau = \frac{m^* \sigma_D}{e^2 n_s}$ 3D $\tau_{3D} = \frac{3D}{(\frac{1}{3})v_F^2}$
Eq 10	Fermi quasi-momentum	2D $k_F = \sqrt{2\pi n_s}$ 3D $k_F = \sqrt[3]{3\pi^2 n_v}$
Eq 11	EEI	$\delta\sigma_{EEI}(T) = G_0 K_{ee} \ln \frac{k_B T \tau}{\hbar}$
Eq 12	WL	$\delta\sigma_{WL}(T) = G_0 \ln \frac{k_B T \tau}{\hbar}$

Table 1. continued

Eq 13	MR	$MR \equiv \Delta R/R(0) \equiv (R(B) - R(0))/R(0)$
Eq 14	MC	$MC \equiv \Delta\sigma/G_0 \equiv (\sigma(B) - \sigma(0))/G_0$
Eq 15	Mean free path	$l = \sqrt{D\tau}$
Eq 16	VRH	$R_s = R_0 e^{\left(\frac{T_0}{T}\right)^p}$
Eq 17	HLN1	$\frac{B}{B_{tr}} \ll 1$ $MC = \left[\psi\left(\frac{1}{2} + \frac{B_\phi}{B}\right) - \ln \frac{B_\phi}{B} \right]$
Eq 18	HLN2	$MC = \left[\psi\left(\frac{1}{2} + \frac{B_\phi}{B}\right) - \psi\left(\frac{1}{2} + \frac{B_{tr}}{B}\right) - \ln \frac{B_\phi}{B_{tr}} \right]$
Eq 29	HLN3	$MC = \left[\psi\left(\frac{1}{2} + \frac{B_\phi}{B}\right) - \ln \frac{B_\phi}{B} \right] - D \left[\frac{B^2}{1+(mB)^2} \right]$
Eq 20	Measured conductivity	$\sigma(T) = \sigma_D + \delta\sigma_{WL}(T) + \delta\sigma_{EEI}(T)$

2. METHODOLOGY: GEOMETRY AND SETUP

2.1 Van der Pauw geometry

The Van der Pauw geometry describes the arrangement or placement of 4-point contacts to measure the resistance of a thin film. The contact placement depends on the sample shape. The Van der Pauw geometry used in this paper for comparative analysis is the square configuration with

contacts in the corners as seen in figure 4. When the samples have contacts deposited on them care is taken to ensure the

contacts are as close to the outside edge as they can be placed without shorting the sample. For the Van der Pauw technique to work, the structure must be of negligible and uniform thickness (as compared

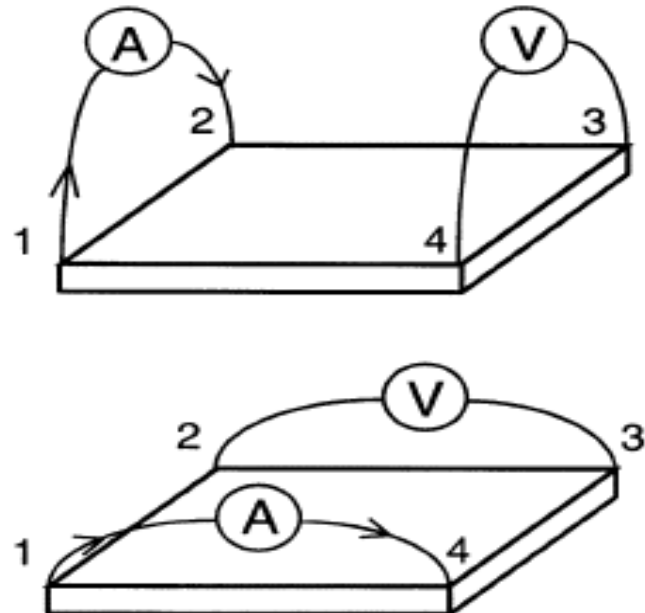


Figure 4. Van der Pauw geometry. is an image of the Van der Pauw structure with numerical markings to indicate the exact measurements used in this research

to the area of the structure) and be homogenous in composition. Although it is not required that the structure is symmetrical, obtained results are more accurate on highly symmetric samples. Most important for the Van der Pauw technique is that the contacts are placed on the perimeter of the structure and be much smaller than the area of the structure³⁷. For verification of the sample geometry, the direction of the current is

reversed and then averaged over both current directions. Offsets in the source and meter are canceled out by this approach and the systematic measurement error is reduced. The magnitudes of the forward and reverse polarity voltage measurements should be close but if they differ greatly then a comparison of all the configuration will give a good aid in debugging the test setup³⁷. The spacing between the contacts and the sample edge (d) and the spacing distance from one contact to another (D) as seen in figure 5

are very important factors in keeping the measurement error low. To keep the error less than 1% a ratio of $d/D=.048$ is needed³⁸. For samples that are not perfect squares, the voltage to current ratio is slightly different for the measurement configuration shown in figure 4, with larger resistance values measured along the long sides of the sample. The ratio of the average resistance values obtained along both sides of the sample can be used to determine a correction factor to determine the sheet resistance from the measured voltage to current ratios R_a and R_b

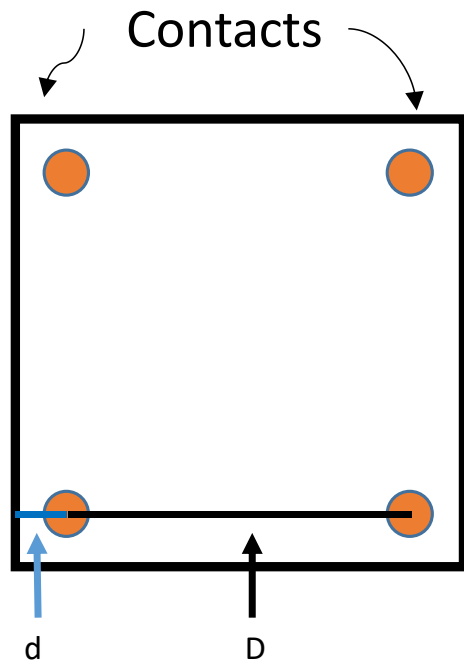


Figure 5. Van der Pauw contacts. The spacing between the contacts and the sample edge (d) and the spacing distance from one contact to another (D)

$$R_a = R_{43} = \frac{V_{4,3}}{I_{1,2}}$$

$$R_b = R_{23} = \frac{V_{2,3}}{I_{1,4}}$$

Alternatively, the measured Ra and Rb values can be used to solve for the sheet resistance Rs using the following equation $e^{\frac{-\pi R_a}{R_s}} + e^{\frac{-\pi R_b}{R_s}} = 1$. The Rs value is calculated using the iterative method to solve the previous equation. The R_{xx} value is the average of all the resistance that the current and the voltage were measured in plane with one another. The R_{xy} term is the average of all the resistances where the current and the voltage were perpendicular to one another.

$$R_{xx}(\Omega) = \frac{R_{12} + R_{21} + R_{23} + R_{32} + R_{34} + R_{43} + R_{41} + R_{14}}{8}$$

$$R_{xy}(\Omega) = \frac{R_{13} + R_{31} + R_{24} + R_{42}}{4}$$

The R_{xy} value is needed to obtain the carrier concentration and the mobility

$$n_s = \frac{1E-8}{e\left(\frac{R_{xy}(\Omega)}{B(T)}\right)} = (cm^{-2})$$

$$\mu = \frac{(-1E8)\left(\frac{R_{xy}(\Omega)}{B(T)}\right)}{R_s(\Omega)} = \left(\frac{cm^2}{V*s}\right)$$

2.2 Electronics

The PPMS is a Quantum Design Evercool 1 system which maintains a 100 Liter Liquid Helium reservoir. This reservoir is used to cool the sample space from 2 to 300K as well as cool a 9Tesla superconducting magnet shown in figure 6. The

magnetic field is perpendicular to the standard sample mounting, but with the addition of

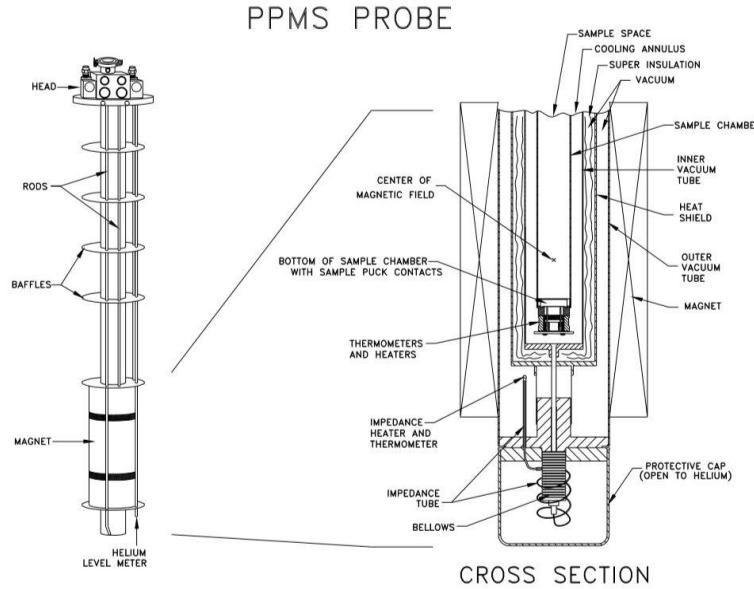


Figure 6. PPMS probe. A cut section of the ppms with magnet and sample orientation

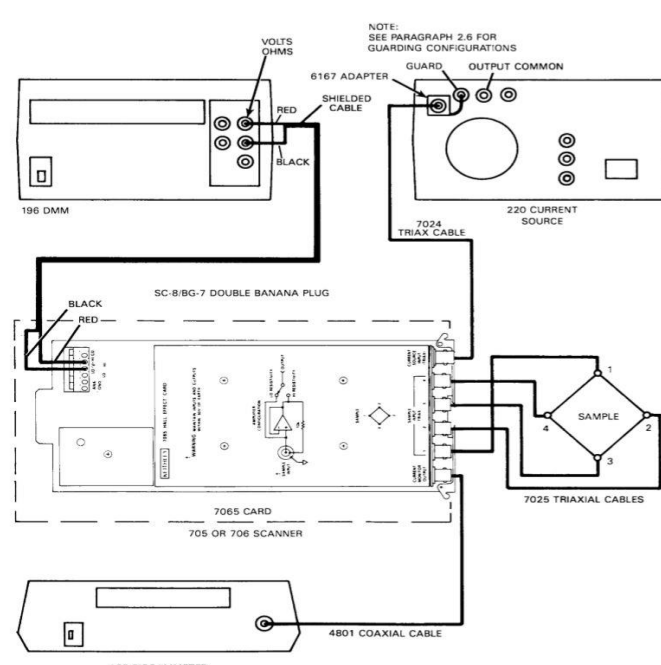


Figure 7. Keithley 7065 hall effect card schematic. A schematic of the electrical connections to the 7065 hall

a secondary component (Horizontal Rotator), the sample can be orientated (0-360degree) to the field. The magnetic field and temperature control are coupled with a Keithley 6221 current source, 7001 switching matrix, 7065 Hall effect card, and 2182A nanovoltmeter. The setup is controlled by a

customized

LabVIEW code to perform the desired measurement. More specifics on the setup including the connections to the sample are shown in figure 7. The 7065 card is installed

inside of the 7001-switching matrix and uses internal relays to change the connection

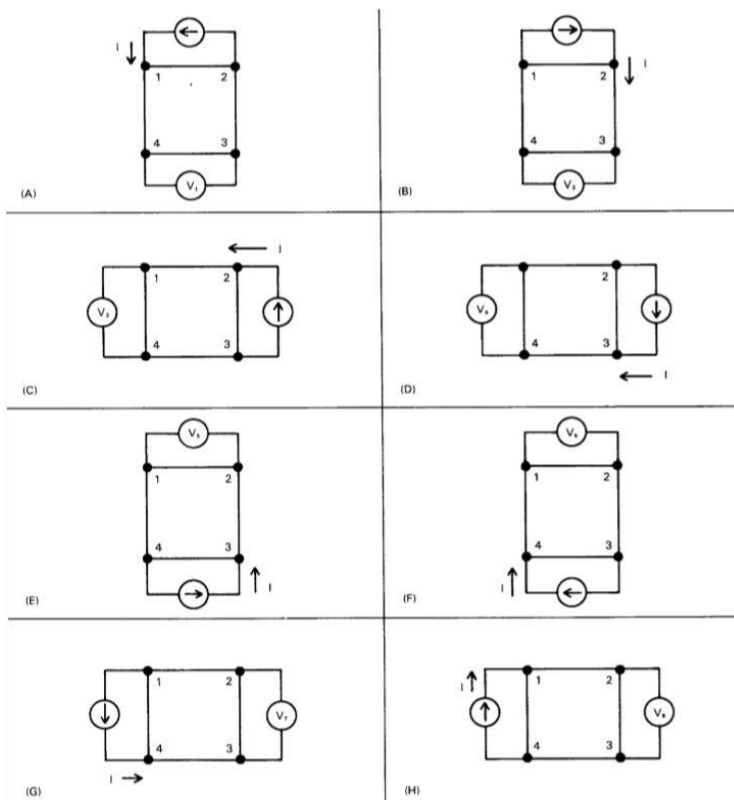


Figure 9. Van der Pauw channels. The 8 different channels (configuration) that are needed for sheet resistance measurement

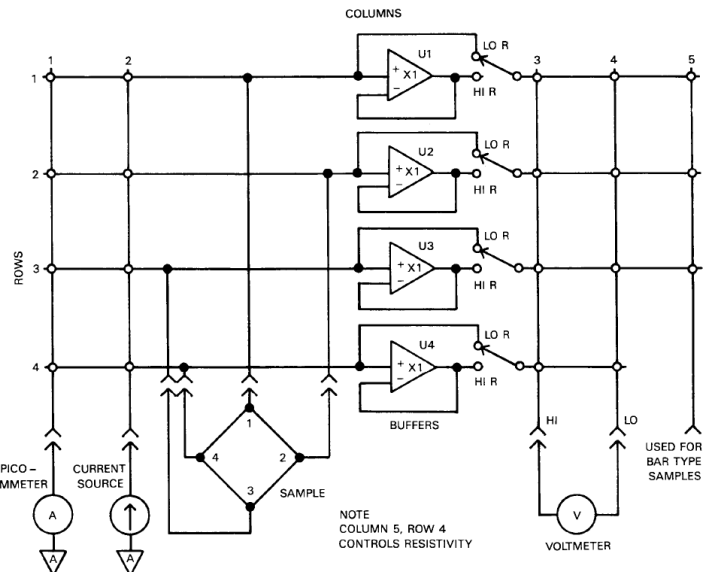


Figure 8. Van der Pauw schematics. Show the wiring of the built-in buffer amplifier of the 7065 hall effect card

configuration. The 7065 card has built-in buffer amplifiers shown in figure 8 which allows for the changing between high and low resistivity mode. The low resistivity setting has an input impedance of 10 Giga Ohms while the high resistive option has an input impedance of

100 Terra Ohms. The low resistivity mode is used to measure samples that have a resistance value below 1 Giga Ohms. For samples with a higher resistance, the use of the high resistivity mode is

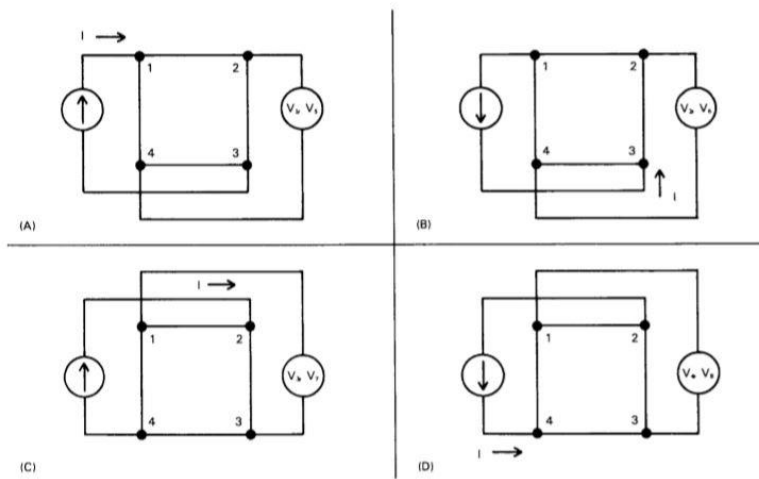


Figure 10. Hall channels. The 4 different channels (configurations) needed for hall measurement.

needed to avoid the voltmeter from shorting the sample. The switching matrix takes four inputs and changes their configurations to match the 12 required channels that are needed to perform the DC Van Der Pauw measurements shown in figures 9 and 10. The configurations in figure 9 show the 8 different orientations needed for sheet resistance measurements and figure 10 shows the 4 orientations needed for hall measurements. The LabVIEW program allows for the input of multiple different temperature set points along with a variety of different magnetic field sweep patterns. The program drives the system to the set temperature allowing for an adjustable time to obtain thermal equilibrium. The system will then use a driven magnetic field control to sweep through the user-defined field parameters. The system stops at each field point where the switching matrix calls a configuration, turns on the current source to the first set current, and measures the voltage. Additional measurements are made at two more current values after which the measurement configuration is changed. This procedure is repeated until the system has completed 12 configurations at which point it moves to the next field point.

2.3 Hall bar measurement setup

The hall bar measurement uses the same system with a very similar setup to that described in the previous sections. The switching matrix can only handle a 4-wire input, but the hall measurement is a 6-wire technique. The switching matrix is connected to the points at which the voltage will be measured shown in figure 11. The current source and sink are connected directly to the Keithley 6221. The same LabVIEW code is used to operate the new setup, but it calls a different set of channel configurations which are custom made for the hall bar structure. Instead of running 3 different currents the system runs positive and negative currents of the same magnitude. This gives the same effect as switching the source and drain without requiring a larger switching matrix.

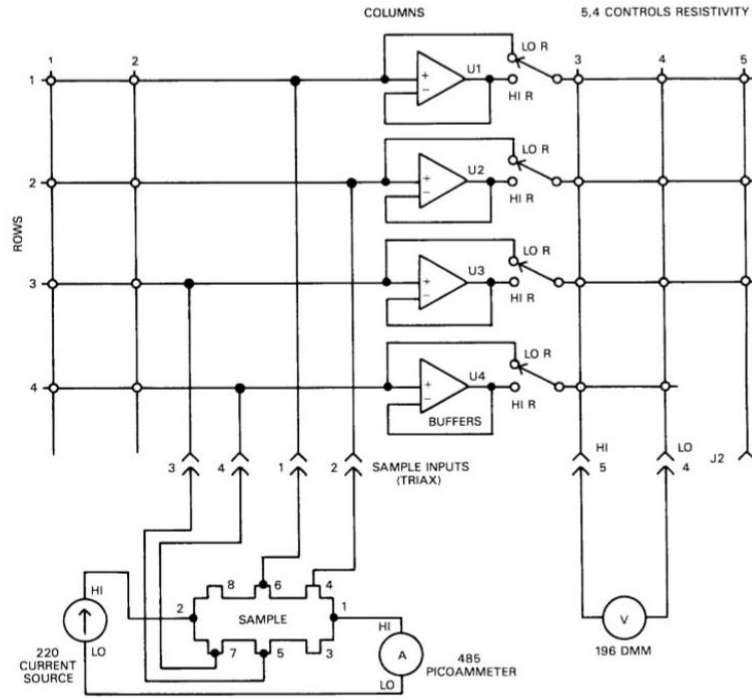


Figure 11. Hall schematics. The electrical connection of the hall bar to the 7065 hall effect card

3. GROWTH AND CHARACTERIZATION OF SrTiO₃ FILMS ON Si

All samples that were grown in the Molecular Beam Epitaxy facility at Texas State

University by Dr. Ryan Cottier.

The SrTiO₃ films were grown silicon (Si) (001) substrates via oxide Molecular Beam Epitaxy (MBE) using Ti and Sr effusion cells for co-deposition with a base pressure of $\sim 10^{-10}$ Torr and an O₂ partial pressure of $4 \times 10^{-8} - 4 \times 10^{-7}$ Torr

resulting in slightly Oxygen deficient films. The surface quality and stoichiometry were monitored continuously using *in-situ* reflection high-energy electron diffraction. The growth temperature was 500 C and the exact growth procedure including the Si de-oxidation process is described in ³⁹. All samples are Ti-terminated and were not annealed post-deposition. The thickness of these single-crystal (001) SrTiO₃ films on Si was 20 nm, and the films were almost fully relaxed. They are characterized using SEM, XRD, and AFM. This characterization process is for determining the quality of the growth. Using the SEM there are 3 common defects that can be identified: incomplete cleaning before growth, TiO₂ Nucleation, and STO Nucleation all shown in figure 12. A good growth will look like a blurry image in the SEM figure 12 (bottom right) as it is atomically flat with no

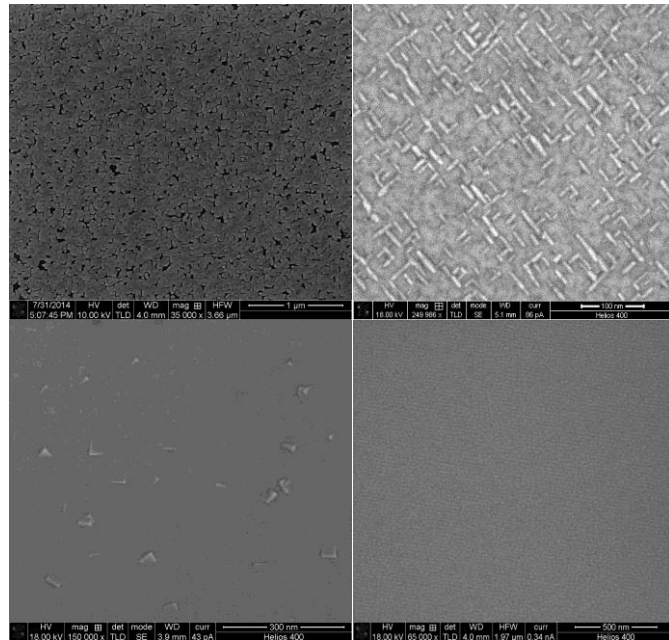


Figure 12. SEM images. SEM images of TiO₂ Nucleation (Top Left), STO (011) Nucleation (Top Right), Incomplete Nucleation or Cleaning (Bottom Left), Epitaxial growth (Bottom Right)

features to focus on and is shown in the bottom right corner of figure 12. The AFM scan shown in figure 13 gives the surface roughness of the samples after they have been grown. The roughness for all the samples used in this study are on the order of 1E-10m.

The third characterization technique used is XRD and can determine the crystallinity of the films, grain size and epitaxial orientation. The following four measurements provide similar results between samples; the scans shown are representative of the entire set. The

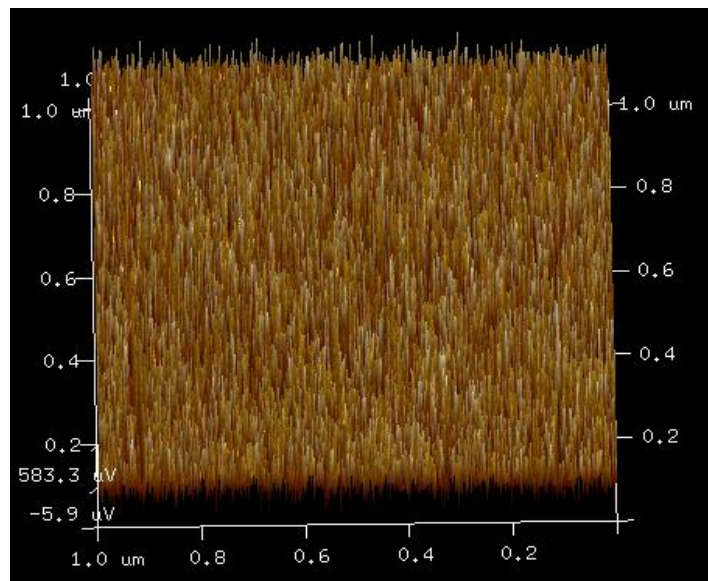


Figure 13. AFM scan. Surface roughness scan of 161206-01 with an Ra value of 1.7E-10

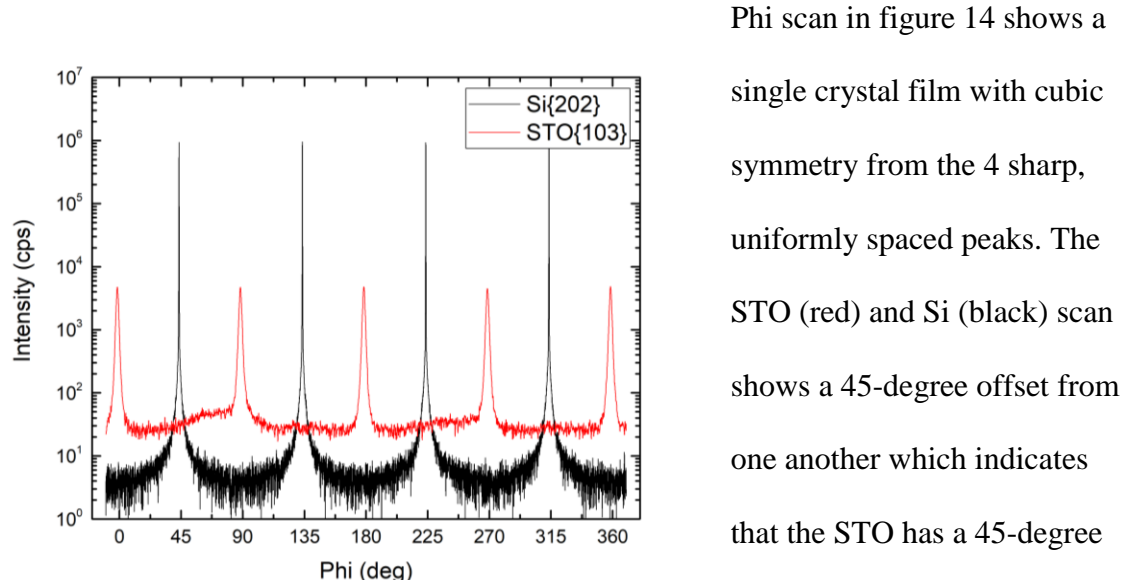


Figure 14. Phi scan. The phi scan shows a cubic lattice from the 4 uniformed peaks which shows evenly spaced vertices. The peaks of the Si (black) and STO (red) are 45 degrees offset from each other which shows 45-degree rotations of the cubic lattice

Phi scan in figure 14 shows a single crystal film with cubic symmetry from the 4 sharp, uniformly spaced peaks. The STO (red) and Si (black) scan shows a 45-degree offset from one another which indicates that the STO has a 45-degree rotation to the surface normal

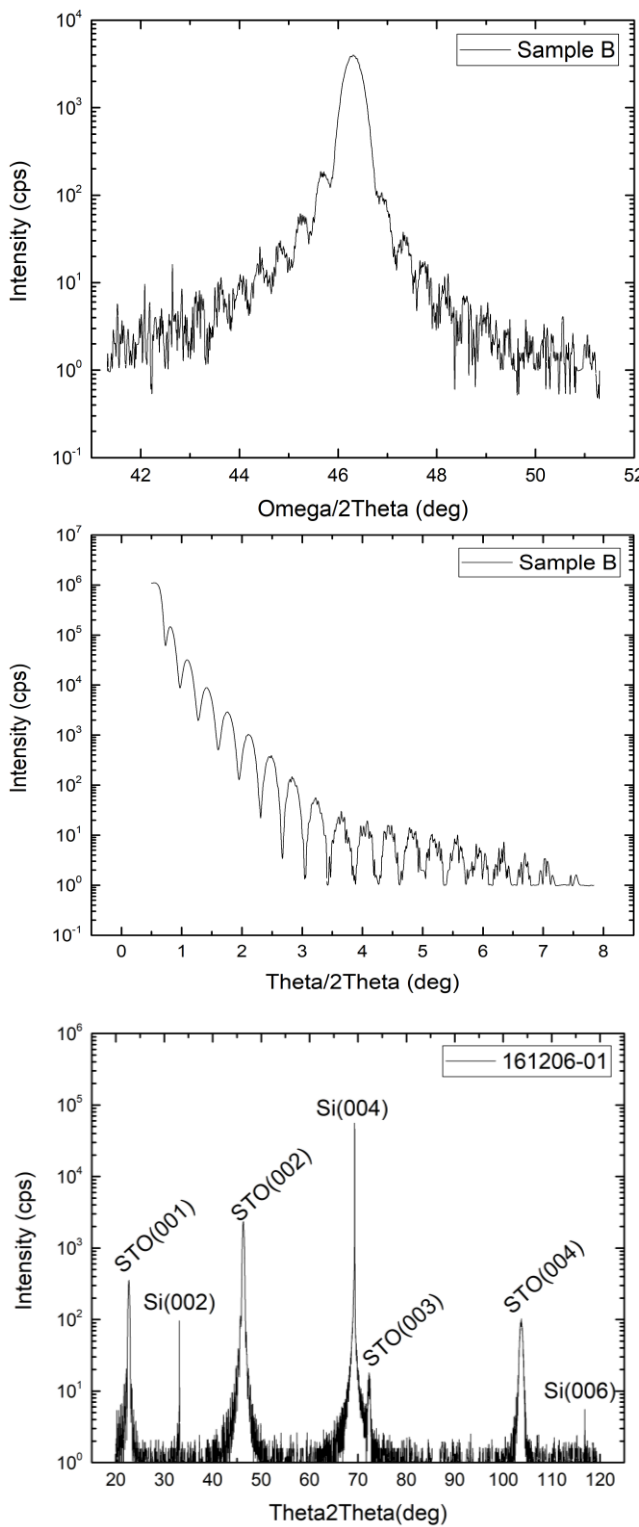


Figure 15. XRD scans. The Omega/2Theta coupled scan (top) The XRR Scan (middle) the survey scan of STO/Si (bottom)

of the Si substrate. The symmetric survey scan in figure 15 (bottom) confirms pseudomorph growth and good alignment between the film and substrate; the c-lattice family of planes (001) for both are parallel with minimal offcut. The Omega/2Theta coupled scan of the STO (002) peak in figure 13 (top) gives the crystal thickness; this matches the measured film thickness from the XRR scan in figure 15 (middle) verifying a single phase, thus confirming single crystallinity.

Table 2. Sample growth parameters

MBE Samples	STO thickness	Rate	O2 pressure	substrate	Substrate resistivity
	nm	nm/s	torr		Ohm-cm
160523-01 Sample A	19.9	.16	4E-8	p-type (100)	5-10
161206-01 Sample B	23.6	.28	4.6E-8	p-type (100)	1-5
161207-01 Sample C	21.5	.25	4.5E-8	p-type (100)	.1-.5
161208-01 Sample D	21.2	.24	5.3E-8	p-type (100)	5-10

4. NANOFABRICATION OF HALL BAR

4.1 Process overview

Dr. Ryan Cottier grew all the thin films using the Texas State University Multiuser Molecular Beam Epitaxy (MBE). The samples are then mechanically cleaved using a diamond scribe into 8mm by 8mm squares. The samples are transported to the NRSS (Nanofabrication Research Shared Space) clean room facility. All photolithography work is completed in the specified “Litho” area in the clean room as all the lights in the area have been filtered to wavelengths (585-620 nm). The S1813 photoresist used in processing is exposed at 300 nm -500 nm wavelength so ensuring that the ambient room light does not affect the processing is very important. The square pieces are cleaned using the spin coater in the clean room with acetone first and then rinsing with IPA. The spin coater uses a vacuum chuck to hold the sample in the center while rotating the sample at a programmed RPM, acceleration, and spin time. The parameter of the spin program will vary depending on the desired film thickness, the substance being spun, and the surface being covered. To ensure that the surface of the sample is completely free from any residual chemical, the samples are placed in a vacuum oven set to 100-degree C and a vacuum level of 558 Torr. The samples are removed from the vacuum oven and allowed to cool for 30 minutes before proceeding. Each different type of photoresist has a

documented Spin Speed Curve figure 16 which gives you the average film thickness given different spin speeds in rpm for various photoresists. This curve provides the starting point for creating a spin program to obtain a desired final thickness.

A challenge when spinning photoresist is roll off, the

thickness of the center will be thicker than the thickness along the edge due to the centripetal force having a stronger effect further away from the center of rotation. Roll off can be minimized using a few different techniques such as using a multiple step spin speed or using smaller samples. As the samples investigated in this thesis are square and have a size of only 8mm by 8mm a multiple spin speed approach was not necessary to keep the roll off to $\sim 100 \text{ \AA}$ (Angstroms). After several, different sample runs it was found that with a setting of (speed:4000 rpm acc:2000 rad s $^{-2}$ time:15 seconds) a final thickness of $13000\text{\AA} \pm 1000\text{\AA}$ could be obtained. If for any reason the thickness is outside this range or the film has a defect, the sample can be reworked. The sample is placed into the spin coater and 5mL of S1813 is prepared in a disposable pipette for dispersion onto the surface. The resist is dispensed onto the surface of the sample before the spinning program is started. When applying the resist, it should pool on the sample surface of the sample without running over the sides. The film thickness can be affected by the shape

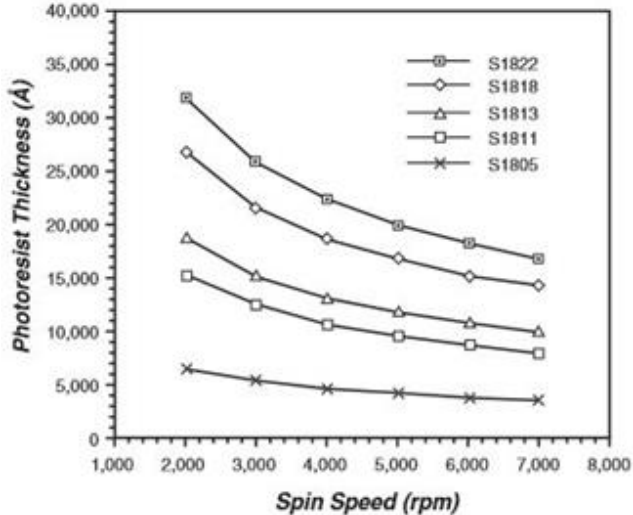


Figure 16. Photoresist Spin Speed Curve. The curve gives the average film thickness for different photoresists at given speed in rpm

and size of the sample, surface roughness, the material on the sample, the viscosity and age of the photoresist, and the method of application. After the Photoresist is applied to the surface of the sample, the sample is soft baked for 60 seconds on a 100-degree hot plate. The Brewer CEE-1300x gives a 0.1-degree C temperature resolution and a 0.3% uniformity across the surface. The soft bake step is needed to outgas the resist so that it does not stick to the mask in later steps. The bake needs to take place on a hot plate because if it is performed in an oven the air temperature creates a skin on the surface of the resist and it will not outgas properly. Once the sample has been baked it is removed from the hot plate and its film thickness is measured using the Filmetrics UV-20. This system determines the film thickness of the photoresist from the reflection spectrum.

Baseline measurements are conducted on a known Si substrate so that the system can remove ambient light interference and calibrate the system. Once the baseline is set a structure needs to be specified modeled as air/S1813/Si

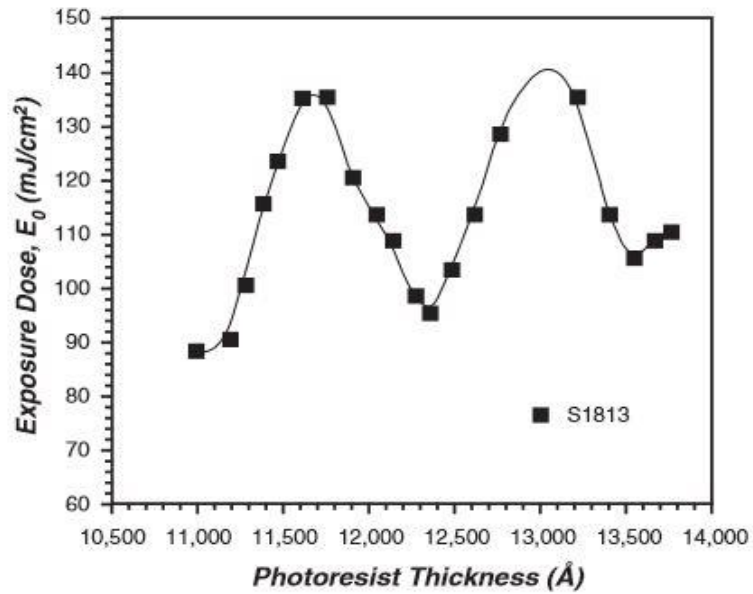


Figure 17. Dose to Clear (DTC). the required dose to completely clear S1813 photoresist of different thickness.

so that the system can measure the thickness of S1813 on top of the samples. Once the film thickness is known, the Dose to Clear (DTC) can be extracted from the S1813 Photoresist Interference Curve figure 17. The curve only covers the range of 11k-13.7k

\AA ; if the sample thickness is outside of this range then the sample will need to be stripped of photoresist and processed again. If the thickness is within range, then the Exposure Dose can be determined from the curve and can be used to calculate the exposure time needed to reach the required exposure dose. The SuSS MJB4 mask aligner is used to place the sample into adjustable levels of contact with a mask which holds the desired pattern to be transferred to the sample. The light source on the mask aligner has an output of $\frac{mW}{cm^2}$ the DTC is given in $\frac{mJ}{cm^2}$ so to obtain the necessary exposure time it is necessary to divide the DTC by the baseline exposure of the mask aligner. To find the baseline of the mask aligner a plain Si sample is placed in the system and the light intensity is read from the light source during operation. When the sample covered with photoresist and the mask has been loaded, the sample can be translated a small distance (x,y, and z) to allow for alignment of multiple process layers. The exposure time and level of contact are set in the parameters. After the samples, has been exposed to light using the mask aligner it is moved to the vent hood for developed. The sample is submerged in AZ developer for 60 seconds and then rinsed off with DI water. The sample is then loaded into the sputtering chamber where the Ion miller is used to mill away any material that is not covered by photoresist. The Ion Miller has defined set points on the controller so mill test are performed and logged to find the mill time needed to clear a known film thickness. After milling, the samples are loaded into the Angstrom Engineering E-Beam Evaporator. The system has 2 electron beam sources that have 5 different materials and a third resistive source for Al deposition. A 100 nm layer of SiO₂ is deposited using electron source 1 onto the sample surface. The samples are then removed from the system and placed in the vent hood located in the 1000 class clean room area for a liftoff process. The samples are

submerged in a container of N-Methyl-2-pyrrolidone (NMP) and are allowed to soak for 20 mins. NMP reacts with the photoresist and dissolves it so the additional material on the resist is also washed away. If the lift-off is successful, the only material left is the material deposited directly on the substrate. If the photoresist is not lifting off in areas the NMP is heated to 100 C to improve its effectiveness or the sample in the solution can be sonicated for 10 mins. Sonication is used as a last course of action as it can cause small cracks in the substrate. The sample is removed from the NMP and then rinsed with Acetone and IPA after which they are dried with an N2 gun. The samples are then inspected using an optical microscope to ensure liftoff has been completed and placed back into the NMP container if liftoff is not completed. The samples are then taken back into the Litho bay for the second step of the photolithography process. For the second photolithography layer a new layer of resist is applied to the surface of the sample but this time the spin time should be extended (rpm:4000 acc:2000 time:15) due to the change in the surface being spun on is SiO₂. The thickness of the resist is measured, exposed, and developed using the same steps as before. The sample is then placed back into the sputtering chamber but this time the mill time is only 5 seconds to clear any residual (Scum) layer of photoresist from the surface. The samples are removed from the sputtering chamber and placed back into the E-Beam Evaporator. The E-Beam is used to deposit a metallization top layer onto the surface. The samples are removed, and a second liftoff process is performed in the vent hood.

4.2- Ion Milling

The accelerator grid serves two purposes: 1) to extract the ions from the discharge chamber, and 2) to determine the trajectories of the ions, i.e.

focusing figure 18. The anode is biased to the beam voltage which determines the ion energy that goes to the sample.

A neutralizer can be added to the system. The neutralizer is a hot filament which supplies electrons that are available to neutralize the ions on their way

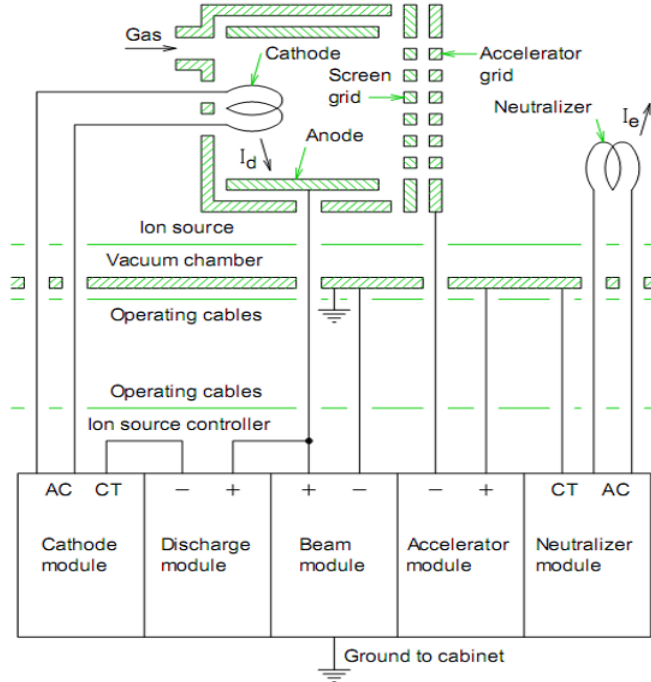


Figure 18. Ion Miller. schematic of Ion miller used in milling process

to the sample. If the neutralizer current is made to be the same as the ion current, the beam can be completely neutralized. Neutralizing the beam does not affect the trajectories of the ions/ neutrals and avoids the sample from charging up. The latter is important as a more homogenous etching rate can be obtained without sample charging distortions. The Kaufman KDC 40 controller has set parameters which control the aggressiveness of the milling process. There is no real-time monitoring of the mill rate and the rate is different for different materials. So, to come up with proper mill times and rates for different materials; the parameters are kept at a set value, which are in table 3, while running test mills. Three samples of a relatively thicker films (40nm) were

prepared and milled for 30, 60 and 90 seconds. After they are milled and removed from the chamber the step height is measured with the AFM. I then take the step height divided by the time to get a mill rate (nm per seconds). I can then use this rate to calculate the time needed to mill through a film of the same material but at different thicknesses. Most of the films that I use are around 23nm which can be cleared by ~90 seconds of Ion Milling if the parameters are kept constant.

Table 3. Ion milling parameters	
Cathode Volts	7.2 V
Cathode Amps	7.74 A
Discharge Volts	44.9 V
Discharge Amps	.86 A
Beam mAmps	43.1 mA
Accelerator Volts	120 V
Accelerator mAmps	2.6 mA
Emission mAmps	44 mA
Neutralizer Volts	9.8 V
Neutralizer Amps	11.5 A

4.3 AFM-Hall bars

AFM scans were used to analyze the Ion milling process and final deposition height. The Ion miller used in processing is kept at predetermined set variables listed in table 3 in the previous section. Mill tests were performed to measure the mill rate of the STO. These mill tests were used to identify the expected mill time needed to clear a known film thickness. From the step height in figure 19, it was concluded that the initial milling process cleared the STO film but went into the substrate by more than twice the thickness of the film.

In the next sample, a thicker layer of SiO₂ was deposited as a verification that the contacts were not shorting to the substrate. Several experiments were required before the milling process was optimized for the samples. During this optimization procedure, the Ion miller experienced several filament failures.

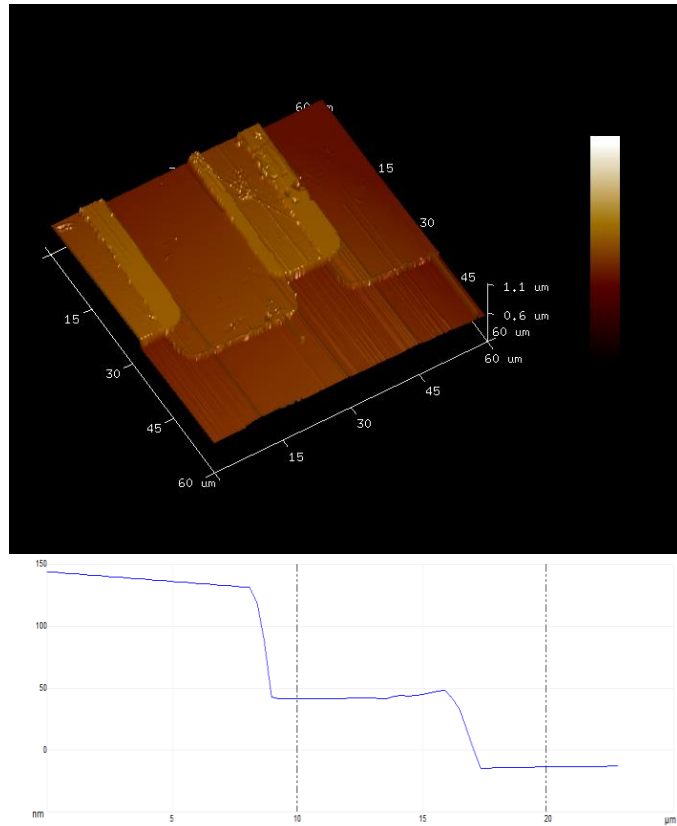


Figure 19. AFM scan of sample B hall. (top) from which a step height is extracted (bottom). The different heights allow for calculating the depth into the substrate the milling achieved

4.4 Deposition

For the processing of the Hall structure, an Angstrom Engineering E-Beam Evaporator was used for the deposition of the SiO₂ electric isolation layer, as well as for the metallization layer. The decision to use the E-Beam Evaporator was made for a variety of reasons including the controllability of the deposition rate, the source materials available, and the processing demand. The E-Beam Evaporator uses two different crystal monitors inside the system for real-time monitoring of the deposition rate and changes in power are made by the computer to maintain the set deposition rate. In the other available deposition technique (sputtering system); the rate is measured at the beginning of a process run and kept at a constant power so that the deposition time needed for a specific film thickness can be calculated. In the sputtering system, it is not possible to monitor the deposition rate in real time and there is no control system in place to maintain a set deposition rate over the course of the process. The rate is measured at the start of the process and then again at the end of the process to ensure the deposition is as accurate as possible. The system has negligible variation between the two measured rates.

4.5 SEM

Upon inspection of the fabricated devices using an SEM, physical defects were observed.

In figure 20 (bottom) we see that there are a few areas that show a glowing effect when compared to the surrounding area. This glowing is believed to be the result of photoresists not being properly cleared before the deposition of the contact layer. This hypothesis was tested by adding a second Ion milling step to remove any potential residual photoresist before the contact deposition. The surface of the Cr in

Figure 20 (top) gives a speckled appearance which after some unexpected Magneto Resistance measurements is believed to be the result of Cr oxide which can be magnetic. Figure 19 shows a Hall bar created with a second milling step and Al/Au contacts to resolve the issues seen in figure 20. In Figure 21 the

SEM images do not show any obviously apparent physical defects but after testing several samples the data indicated that the samples were much more resistive then

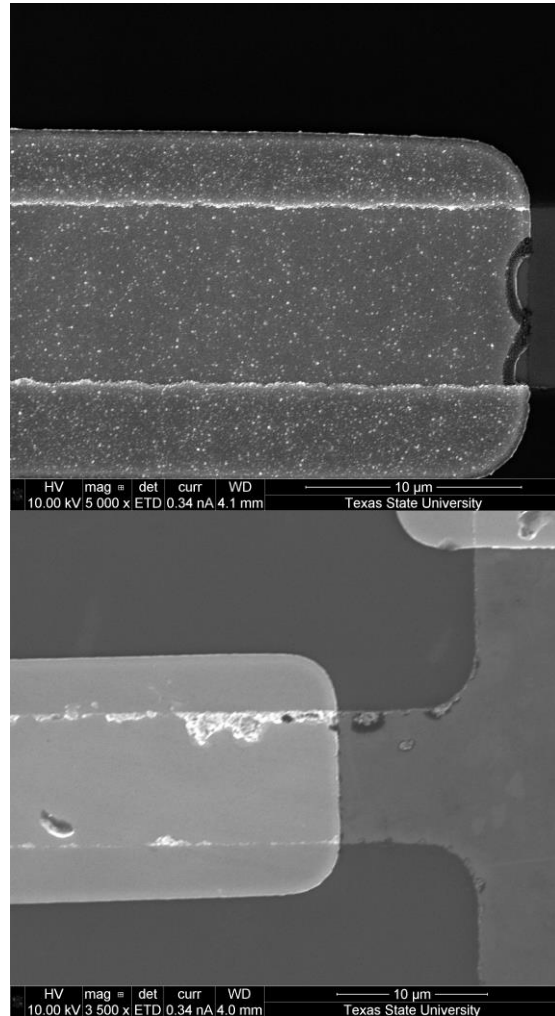


Figure 20. SEM images of Cr contacts on STO. (top) shows a speckled appearance which is believed to be Cr oxide. Al contacts on STO (bottom) shows glowing effects which is believed to be photo resists under the contacts.

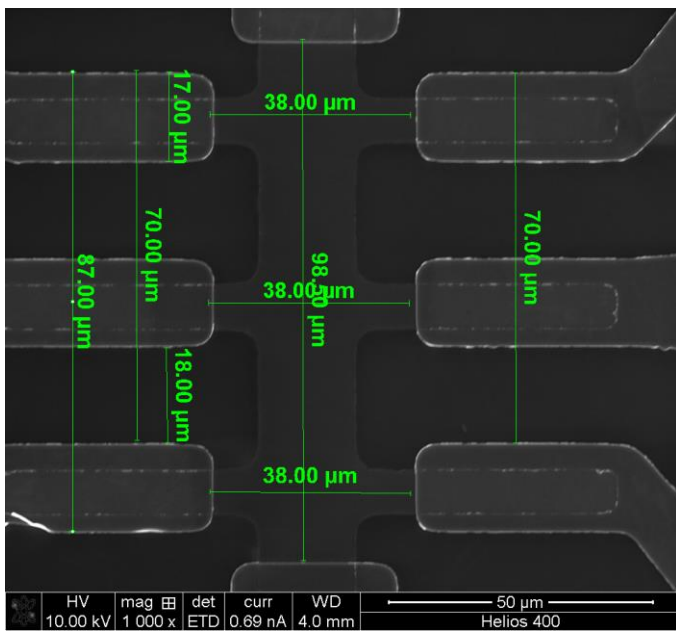


Figure 21. Hall bar dimensions. Al/Au contacts on sample B

measured by VDP technique.

After creating new samples with Ti/Au contacts SEM images show like with the previous sample process there are no obvious physical defects. The Photolithography process can be qualified by how close the dimensions of the Hall bar match the dimensions of the mask. The dimensions do not

have to perfectly match the mask precisely, but the measurement of the dimensions need to be as precise as possible to be used in calculations. The first sample processed had a deviation from the mask of ~11% and the newest samples processed have a deviation of ~4%. Other than the comparison of dimensions we also look at the images to ensure that the lines are well defined and straight.

4.6 Contact metal evaluation

The first consideration for the contact pads material is to deposit a conductive metal that has a work function ($q\Phi$) that is very close to the electron affinity (qX) of SrTiO₃ (STO). When there is a large difference between the electron affinity of the STO and the work function of the metal several things can happen including charge transfer and the formation of a Schottky barrier. The existence of a Schottky barrier will make it difficult to inject current in the sample which will increase the noise in the electronic transport data. The work function of a clean n-type TiO₂-terminated SrTiO₃ surface is around 3.9 eV⁴⁰ and Chromium (Cr) has an electron affinity of 4.5 eV. The .6 eV energy level difference and low oxygen growth make Cr a good choice for making contact to an STO film⁴¹.

5. TRANSPORT ANALYSIS OF SrTiO₃/Si Van der Pauw

5.1 Temperature dependence of R_s

In this chapter, the measurements of the resistance at different temperature and magnetic field are presented for three different samples A, B, and C which are listed in table 1. The sheet resistance shown in figure 22 increases as the temperature is lowered from 300 K to 2 K. In this work, we focus on temperatures below 50 K. The measured sheet resistance is directly related to the conductance by the following equation.

$$\sigma = \frac{1}{R_s}$$

The conductance obtained from the measured resistance is a sum of the classical Drude

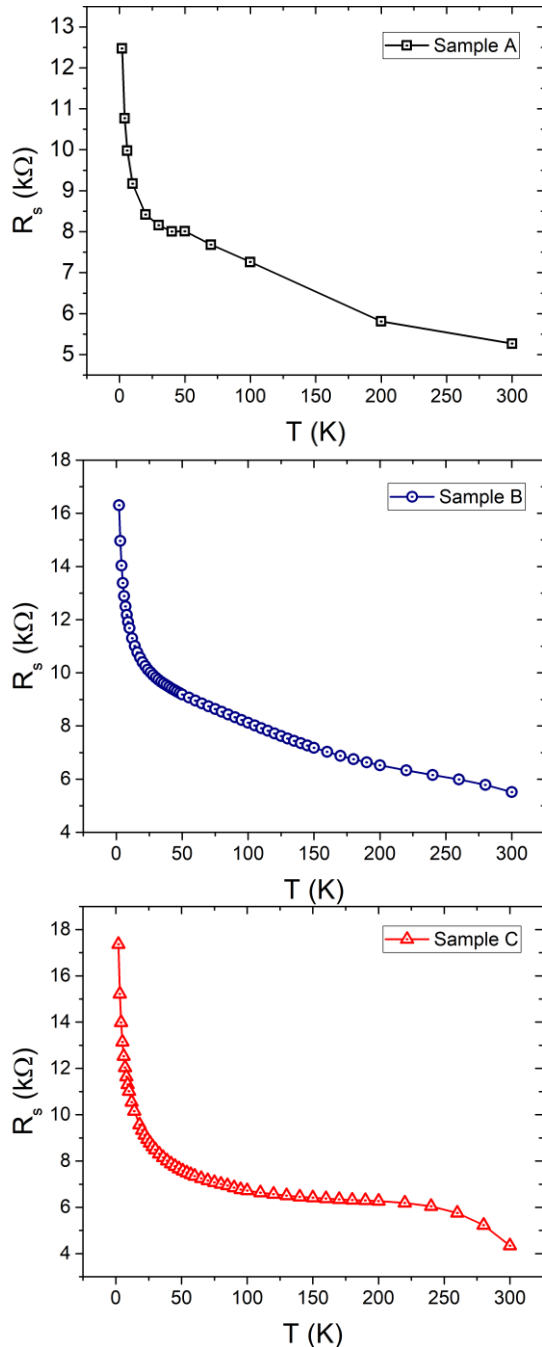


Figure 22. Sheet resistance. 300 K to 2 K for Sample A (top) Sample B (middle) and Sample C (bottom).

conductivity σ_D , and quantum corrections to the conductance, i.e., Weak Localization (WL) $\sigma_{WL}(T)$, and Electron-Electron Interactions (EEI) $\delta\sigma_{EEI}(T)$ equation 22. The Drude conductivity does not change with temperature but the quantum corrections to the Drude conductivity share a $\ln T$ dependency in 2D in the diffusive transport regime as explained in section (1.4). The slope of the $\ln T$ dependence gives the contributions of the quantum corrections following equations 11 and 12. If the slope is 1, the only contribution is WL and any deviation from 1 is the contribution of EEI. The slopes in figure 23 for samples A, B, and C are 1.37, 1.26, and 1.74 respectively which indicate an EEI contribution to the QCC. From equation 11 the slopes give $K_{ee} = .37$ for sample A, $K_{ee} = .26$ for sample B, and $K_{ee} = .74$ for sample C.

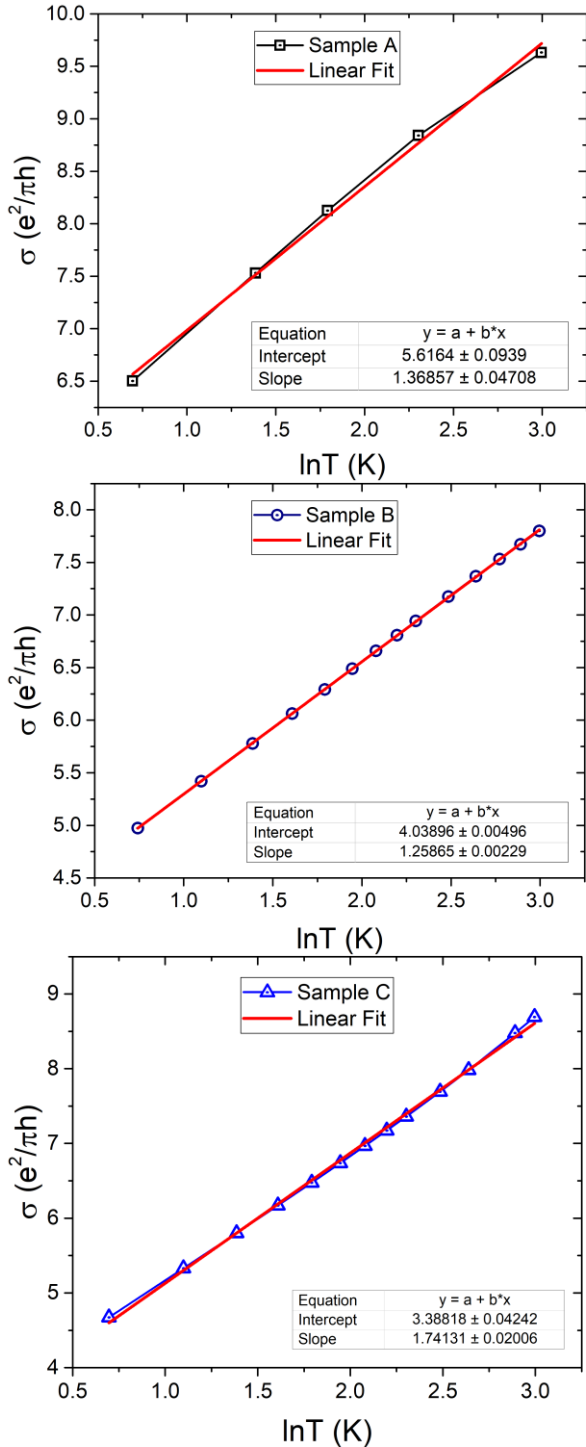


Figure 23. $\ln T$ dependence. conductance divided by the quantum conductance G_0 . Sample A (top) has a slope of 1.37 Sample B (middle) has a slope of 1.26 and Sample C (bottom) has a slope of 1.74.

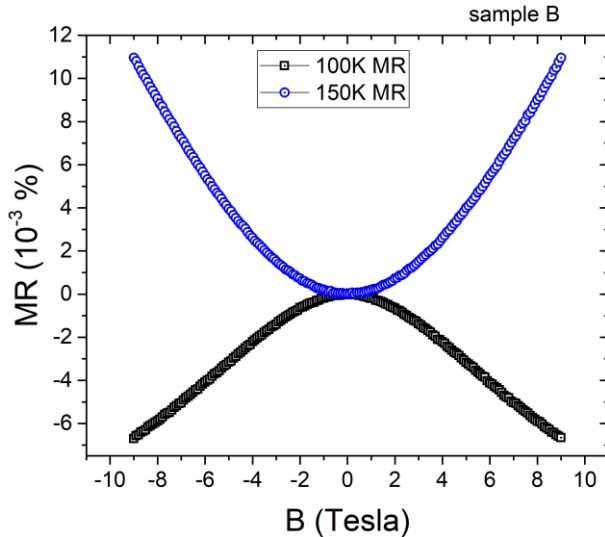


Figure 24. Minimizing QCC. The blue line (top) shows the MR at 150 K and the black line (bottom) shows the MR at 100 K. The scale of the graph has been increased to better see the shift from positive to negative contribution.

positive and the MR at 100 K (black line). The change in the MR sign and the fact that both MR magnitudes are very small indicate that the contribution of QCC is minimized between 100 K and 150 K. The temperature at which the σ_D is estimated is important but it cannot be very precise as at high T phonon contribution contributes to the measurement. In figure 25 the conductance for samples A, B, and C is referenced at a temperature of 100 K point that is used for the estimated σ_D in later calculations.

Another evidence for the manifestation of QCC is the negative MR observed in all samples A, B, and C at 100 K and that increases as the temperature is lowered. The measured conductance is equal to the σ_D where the MR is minimal, which also means that the QCC are minimal. Figure 24 shows the MR at 150 K (blue line) that is

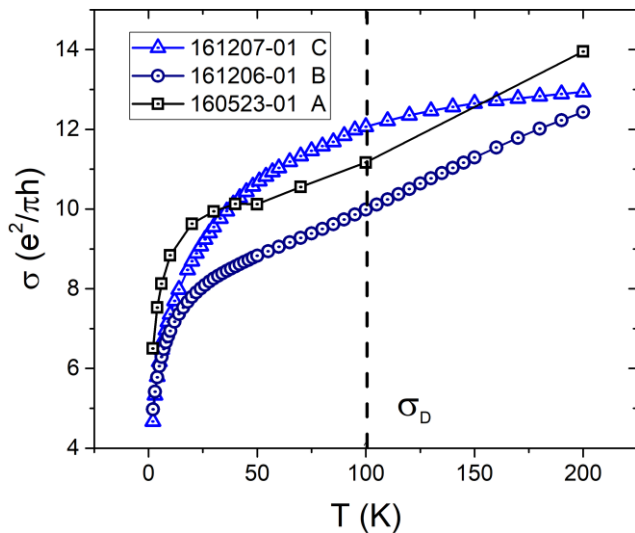


Figure 25: Estimated σ_D . Is taken at 100 K. The graph shows the sheet resistance for sample A, B, and C as they pass the 100 K line.

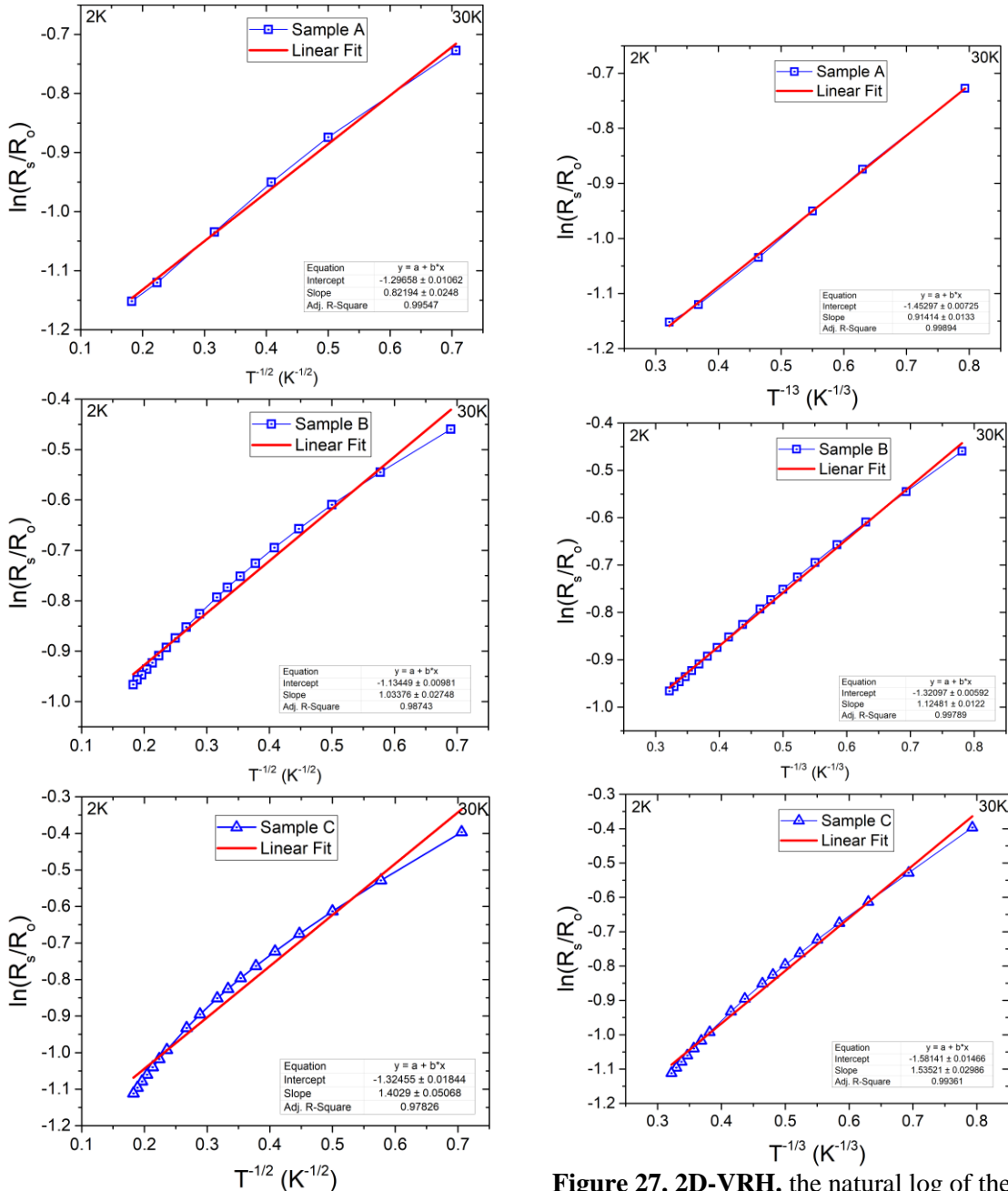


Figure 26. ES-VRH. the natural log of the sheet resistance divided by the quantum resistance on a T to the $\frac{1}{2}$ scale for sample A (left) sample B (middle) and sample C (right).

Figure 27. 2D-VRH. the natural log of the sheet resistance divided by the quantum resistance on a T to the $\frac{1}{3}$ scale for sample A (left) sample B (middle) and sample C (right).

The general expression for VRH is given by equation 16.

$$R_s = R_K e^{\left(\frac{T_0}{T}\right)^p}$$

Where $R_K = \frac{h}{e^2} \approx 25.8 \text{ k}\Omega$ is the quantum resistance, T_0 is a characteristic temperature, $p = \frac{1}{D+1}$ and D is the number of dimensions for D=2 or 3. The plot of

$\ln \frac{R_s}{R_0}$ vs $T^{-\frac{1}{D+1}}$ will show a linear dependence in the appropriate VRH model.

Figure 26 shows the linear fit of $T^{-\frac{1}{2}}$ which is indicating of ES-VRH (Efros-Shklovskii variable range hopping). In this conduction model, the transport characteristics are largely controlled by Coulomb behaviors related to EEI. The $T^{-\frac{1}{3}}$ fitting in figure 27 is indicating of 2D-VRH which is controlled by disorder. The best fit for the collected sheet resistance is the $T^{-\frac{1}{4}}$ fit, shown in figure 28, which indicates 3D-VRH. If the sample obeys 3D-VRH then the transport behavior of the electrons follows 3D kinematic behavior, which may require that the MC be evaluated using 3D equations.

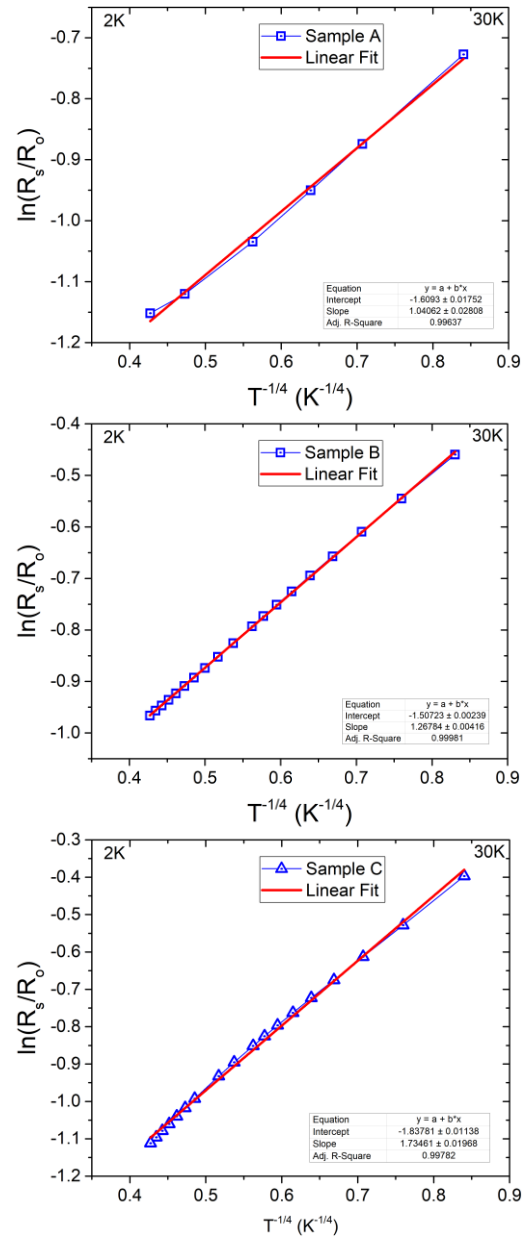


Figure 28. 3D-VRH. the natural log of the sheet resistance divided by the quantum resistance on a T to the $\frac{1}{4}$ scale for sample A (left) sample B (middle) and sample C (right).

5.2 Magnetoresistance

The second characteristic trait of the 2D QCC is negative Magnetoresistance (MR) or positive Magnetoconductance (MC). The measured MR of samples A, B, and C are shown in figure 29 along with the corresponding MC in figure 31. In figure 29 the MR is obtained from equation 4 and is plotted for T= 4 K, 6 K, 10 K, 20 K, 30 K, and 40 K. There is a distinct change in behavior as the system is cooled down, the MR increases in magnitude and remains negative down to 4K. At 2 K as seen in figure 30, the MR is negative up to $\sim \pm 4$ T, it saturates and then increases slightly with the magnetic field. The behavior of the MC in figure 31 shows the inverse behavior of MR. However, MR equation 13 (figure 29)

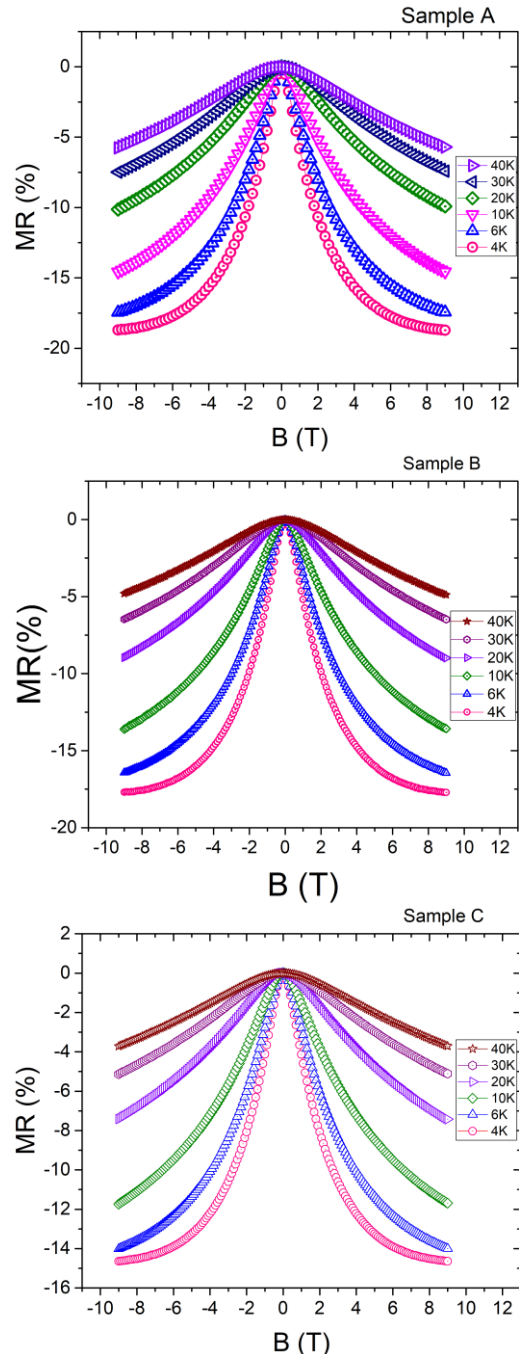


Figure 29. Magnetoresistance. T= 4 K, 6 K, 10 K, 20 K, 30 K, and 40 K for samples A (top), B (middle), and C (bottom). The magneto resistance shows negative contribution

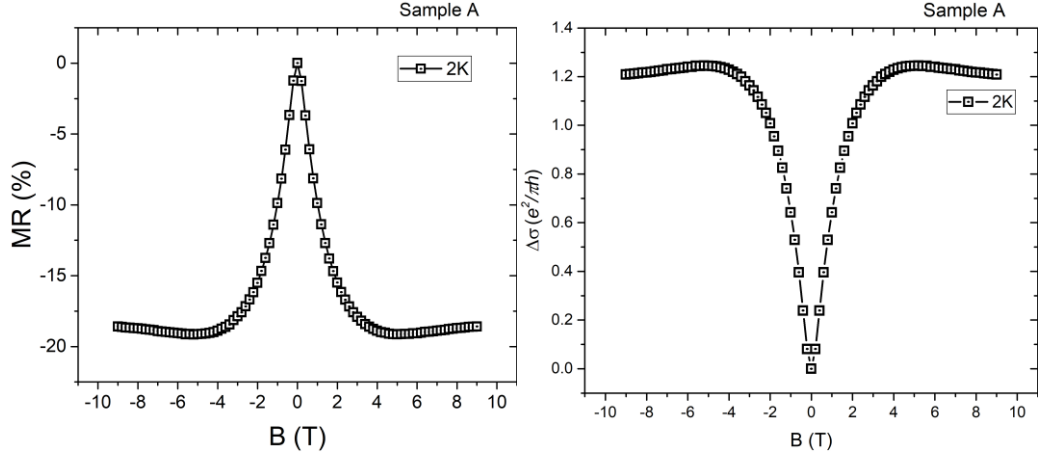


Figure 30. 2 K MR. negative up to $\sim \pm 4$ T and then increases slightly (left). The MC is positive up to $\sim \pm 4$ T and then decreases slightly (right).

and MC equation 14 (figure 31) are not exactly inverse of each other. For the MR the

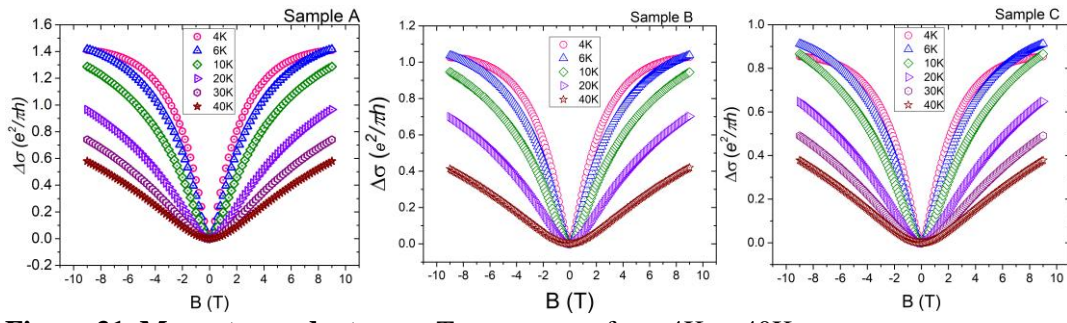


Figure 31. Magneto conductance. Temperatures from 4K to 40K

system is normalized to the zero-field resistance measurement but in MC the system is normalized to G_0 .

5.2.1 MC fitting using the HLN expression with two parameters

The MC in 2D is due to the WL and is theoretically described by the Hikami-Larkin-Nagaoka (HLN) equation (Table 1). The HLN2 equation has two fitting parameters B_{tr} and B_ϕ .

$$MC = [\psi\left(\frac{1}{2} + \frac{B_\phi}{B}\right) - \psi\left(\frac{1}{2} + \frac{B_{tr}}{B}\right) - \ln \frac{B_\phi}{B_{tr}}] \text{ [HLN2]}$$

In the HLN2 equation, B_{tr} is the transport field, characteristic perpendicular magnetic field under which the electron moves in a circle with a radius equal to the mean free path. Similarly, B_ϕ is the phase coherence field, a characteristic perpendicular magnetic field under which the electron moves in a circle without losing coherency, and ψ is the digamma function. HLN2 is used to fit the data using the two fitting parameters of B_{tr} and B_ϕ . The HLN2

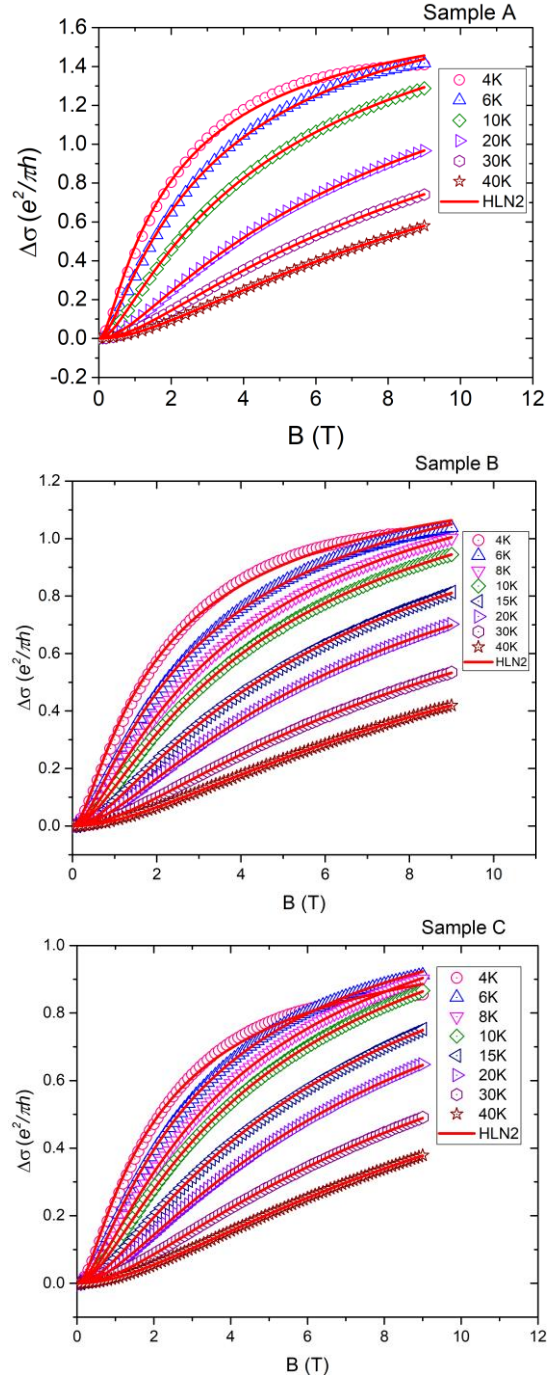


Figure 32. HLN2. The positive magnetic field of the MC at different temperatures for samples A (top), B (middle), and C (bottom) the thick solid red line is the 2 parameter HLN fitting

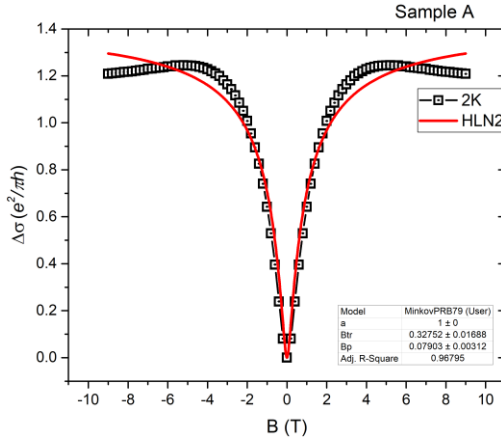


Figure 33. 2K HLN2. The HLN2 fitting doesn't accurately fit the MC at 2 K for the full range of magnetic fields

equation is used to fit the MC at T=40 K, 30 K, 20 K, 15 K, 10 K, 8 K, 6 K, 4 K for samples A, B, and C shown in figure 32. The fitted HLN2 curves are shown by the thick solid red overlaid right on the measured MC represented by the symbols. The fitting at 2 K requires special consideration due to the saturation of the MC. In figure 33 the

two parameter HLN2 fit was applied to the full MC range for T=2 K but it deviates from the data at large magnetic fields and cannot describe the MR saturation. In figure 34 the fitting range of the HLN2 equation was reduced to ± 2 T. The fitting parameters from the

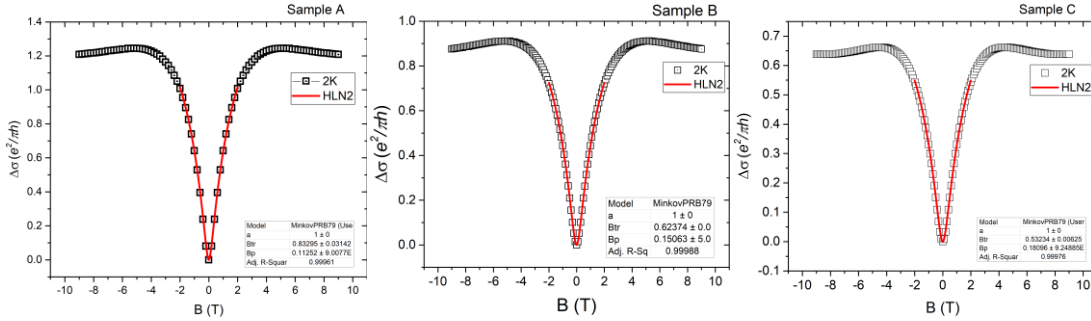


Figure 34. 2K MC HLN2. The MC with HLN2 fit for 2 K on samples A (left), B (middle), and C (right). The fitting range is restricted to ± 2 T

HLN2 fit are shown in figure 35. B_ϕ is increasing with T linearly as expected from the theory in section (1.4) but B_{tr} does not follow the expected behavior. The transport field is not expected to change with temperature since it depends on the mean elastic scattering length/time due to collisions of electrons with impurities or phonons. The transport field is inversely proportional to scattering time and as such the τ_{fit} can be calculated using

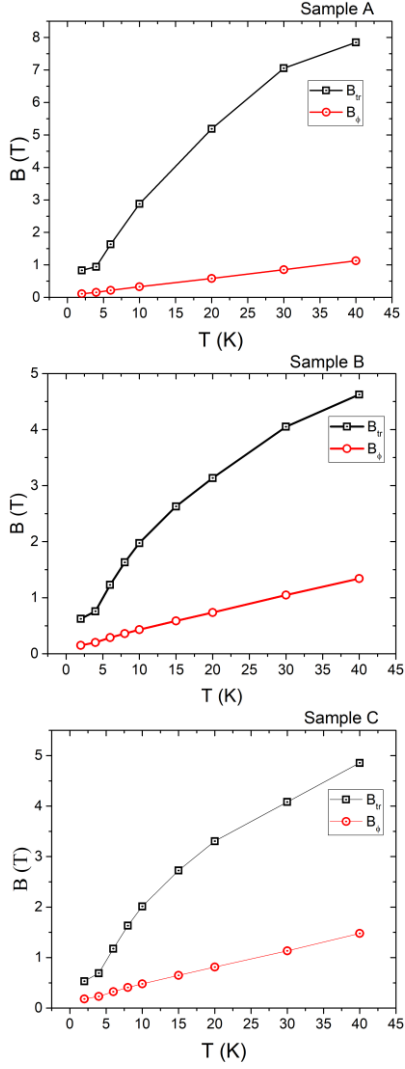


Figure 35. B_{tr} . The two fitting parameters from the HLN equation plotted versus temperature for samples A (top), B (middle), and C (bottom).

time increases as temperature decreases. It seems that the HLN2 fitting is adequate for high temperature but doesn't describe the system well at low temperature.

the transport field obtained from the HLN2 fitting.

Using equation 7 the B_{tr} is used to get the mean free path which along with the diffusion constant equation 5 is used to calculate τ_{fit} .

$$B_{tr} = \frac{\hbar}{2el^2} \xrightarrow{\text{yields}} l = \sqrt{\frac{\hbar}{2eB_{tr}}}$$

$$D = \frac{\pi\hbar^2\sigma_D}{e^2m^*}$$

$$l = \sqrt{D\tau} \xrightarrow{\text{yields}} \tau_{fit} = \frac{l^2}{D}$$

The scattering time τ_{calc} can be obtained using equation 9 with the effective mass of the electron m^* , the Drude conductivity σ_D , sheet carrier concentration n_s , and e.

$$\tau_{calc} = \frac{m^*\sigma_D}{e^2n_s}$$

The plot of both τ_{calc} and τ_{fit} versus temperature in figure 36 shows that below 40 K the difference between the fitted and the calculated scattering

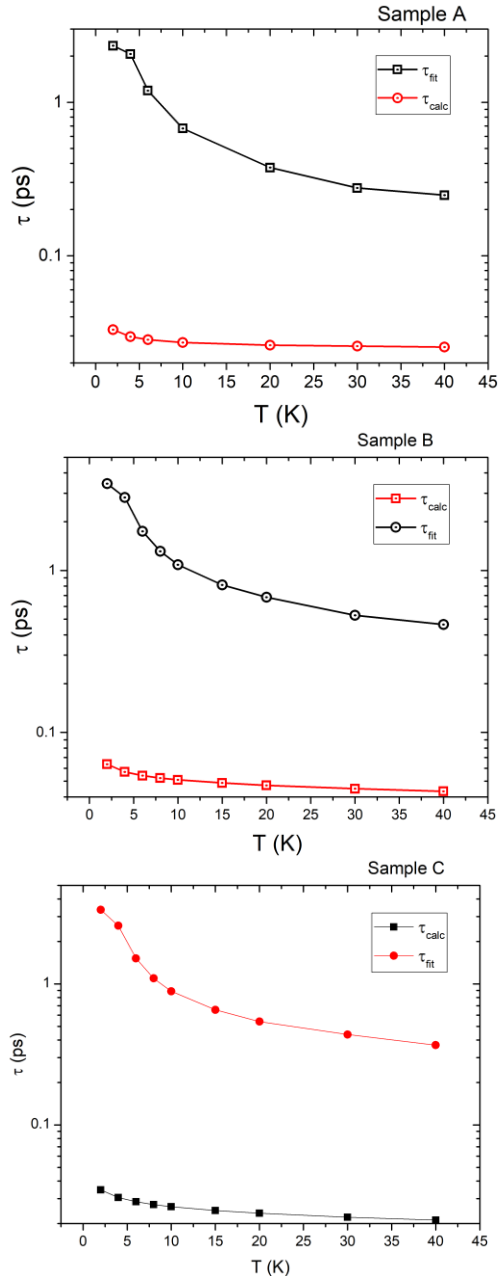


Figure 36. τ_{calc} and τ_{fit} . The calculated scattering time and the scattering time obtained from the HLN equation is plotted versus temperature.

5.2.2 MC fitting using the HLN expression with one parameter

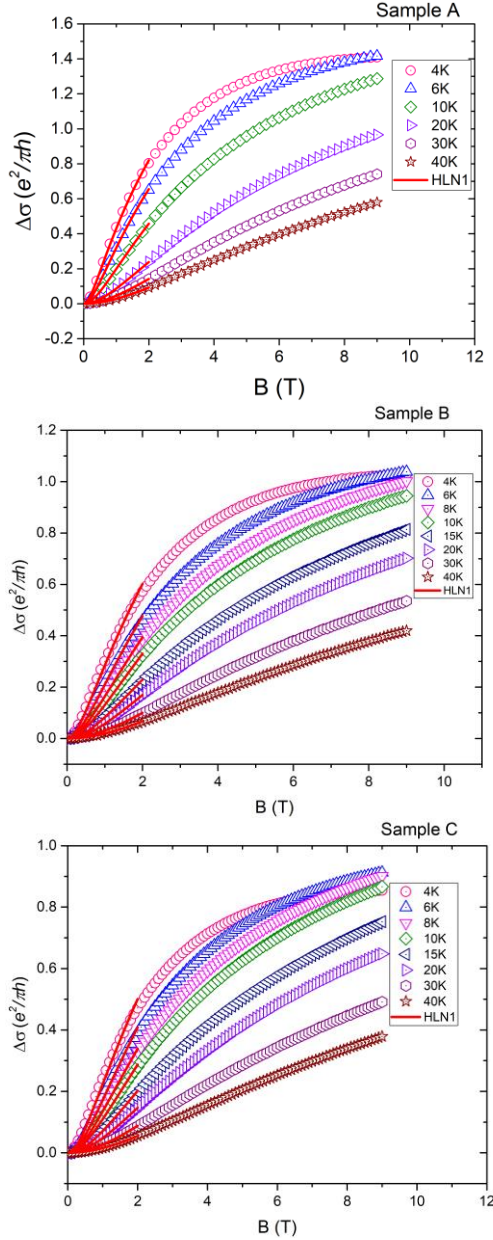


Figure 37. HLN1. The positive magnetic field of the MC. With a 1 parameter HLN fitting for samples

previous fitting figure 37 shows that the HLN1 fitting overlays the MC at low fields. The fitting is restricted to less than 2 T as above this point the transport field begins to

Similarly, to how we calculate the scattering time with the carrier concentration and the Drude conductance; the B_{tr_calc} can be calculated using equations 7, 10, and 1.

$$B_{tr} = \frac{\hbar}{2el^2}$$

$$k_F = \sqrt{2\pi n_s}$$

$$l = \frac{(\sigma_D)}{\pi k_F}$$

The calculated transport field (18.3T) is significantly larger than the fields used in the data. To further assess what the appropriate transport field is the limit is investigated where $B \ll B_{tr}$, $\Psi\left(\frac{1}{2} + \frac{B_{tr}}{B}\right) \approx \ln \frac{B_{tr}}{B}$ and HLN2 reduces to a 1-parameter fit equation HLN1.

$$MC = \left[\Psi\left(\frac{1}{2} + \frac{B_\Phi}{B}\right) - \ln \frac{B_\Phi}{B} \right] [HLN1]$$

Following the same procedures as the

contribute to the data. In figure 38 the fitting of the 2K data is presented and the fitting is restricted to less than 2 T. The values of B_ϕ obtained from the 1-parameter fit closely matches the values obtained from the 2-parameter fit but the fits do have small deviations and cannot fit the data for the full range.

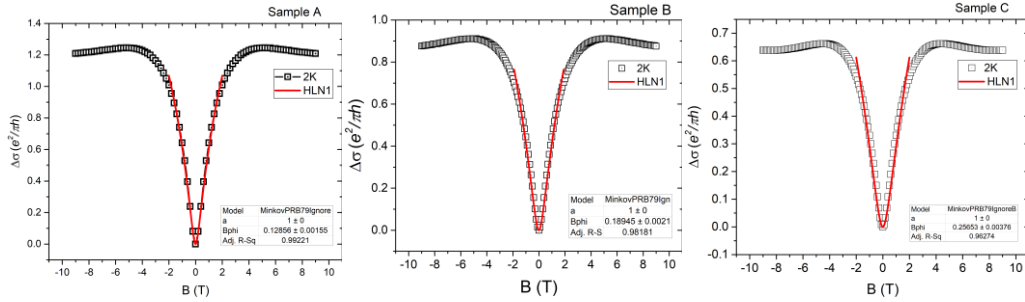


Figure 38. 2K MC HLN1. The MC with HLN1 fit for 2 K on samples A (top), B (middle), and C (bottom). The fitting range is restricted to ± 2 T

5.3 3-D kinematic data

In all the previous equations used to calculate τ , from the carrier concentration or transport field, we were working with 2D equations. From the RvT fitting to the $T^{-\frac{1}{4}}$ the equations need to be changed to account for the possibility that the transport mechanism should be described by the 3d kinematic equations. While QCC describes the MC and s vs T well, the mean free path at 2K is 22 nm, which is much smaller than the phase coherence length. The HLN1 fitting parameters and the calculations for the Diffusion constant will remain the same. To find the τ_{3D} we now need n_v equation 3 the volume carrier concentration, where d is the thickness of the sample, k_F equation 10 the Fermi quasi-momentum, v_F equation 8 the fermi velocity.

$$n_v = \frac{n_s}{d}$$

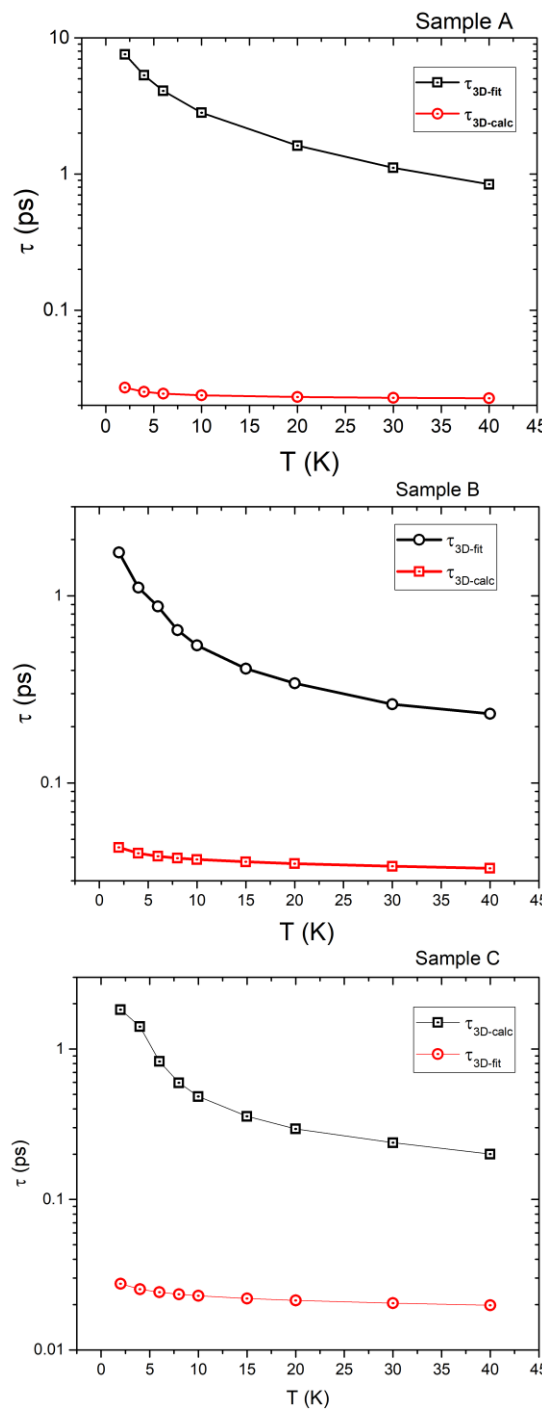


Figure 39. 3D fit. calculated scattering time plotted versus temperature for samples A (top), B (middle), and C (bottom).

$$n_v = \frac{k_F^3}{3\pi^2} \xrightarrow{yields} k_F = \sqrt[3]{3\pi^2 n_v}$$

$$v_F = \frac{\hbar k_F}{m^*}$$

$$\tau_{3D_{fit}} = \frac{3d}{v_F^2}$$

The $\tau_{3D_{fit}}$ and $\tau_{3D_{calc}}$ in figure 39 shows that there is a greater deviation of the scattering time using the 3D equations than using the 2D. Once the calculations are completed with the sample thickness d ; another consideration is that the charge confinement thickness is smaller than the sample thickness. To check this possibility an estimated thickness of 2nm is replaced for the sample thickness to see if the values of $\tau_{3D_{fit}}$ and $\tau_{3D_{calc}}$ show a smaller deviation. Even with using a smaller thickness the deviation using the 3D equations were greater than the 2D system.

5.4 Hall Resistance

The sheet carrier concentration n_s that are used in the previous sections of the analysis are obtained from the slope of the R_{xy} vs. B (hall slope). The Hall slope on figure 40 indicates the carriers by the sign of the slope; electrons cause a negative slope, and holes cause a

positive slope. From the numerical value of the slope, the carrier concentration is identified. The data is antisymmetric across the zero-field point and as such a detailed inspection of the slope can be performed on just the positive field without losing any data for fittings. In figure 41 the difference between the change in $(\delta R_H)_{EEI}$ as a function of

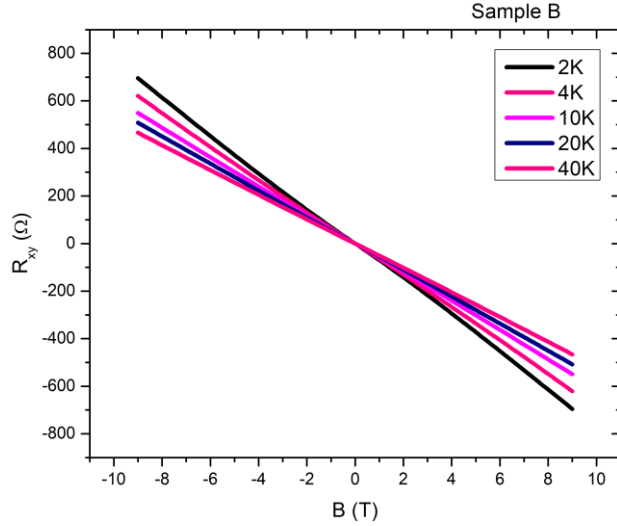


Figure 40. R_{xy} , at different temperature plotted versus magnetic field

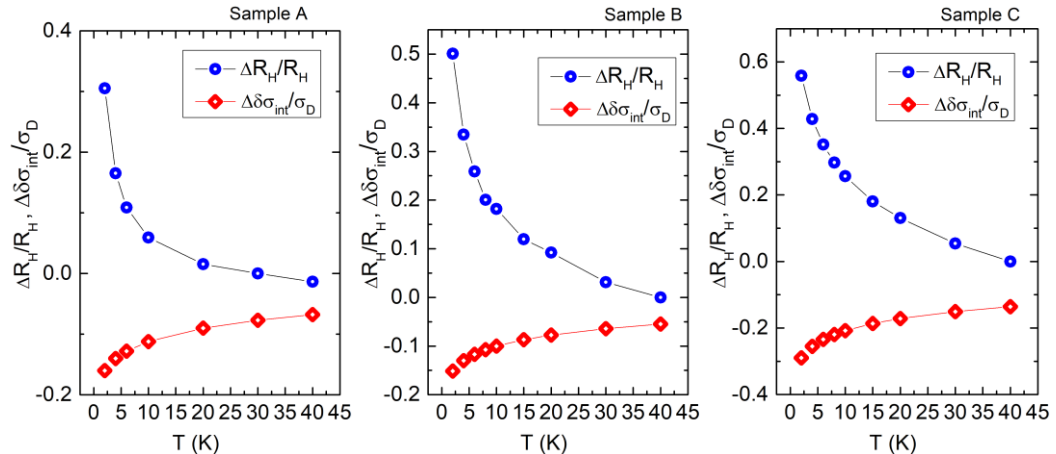


Figure 41. Electron Electron Interaction. Samples A, B, and C follow the expected EEI theory $\frac{(\delta R_H)_{EEI}}{R_H} = -2 \frac{(\delta \sigma_d)_{EEI}}{\sigma_d}$

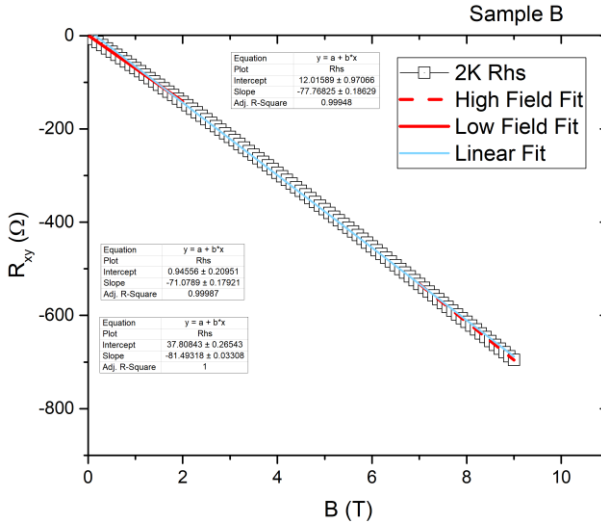


Figure 42. 2K hall slope. The positive field linear fit at low field and high field shows two different slopes. The fit over the full range gives the average slope of both the different ranges.

was plotted for only positive fields in figure 42 which after doing linear fits at low fields (0-2T) and high fields (7-9T) there are two different slopes. The different slopes may indicate that there are more than 1 carries present in the sample and as such the HLN1 and HLN2 equations will not be appropriate to use for the data analyses of the samples. The two

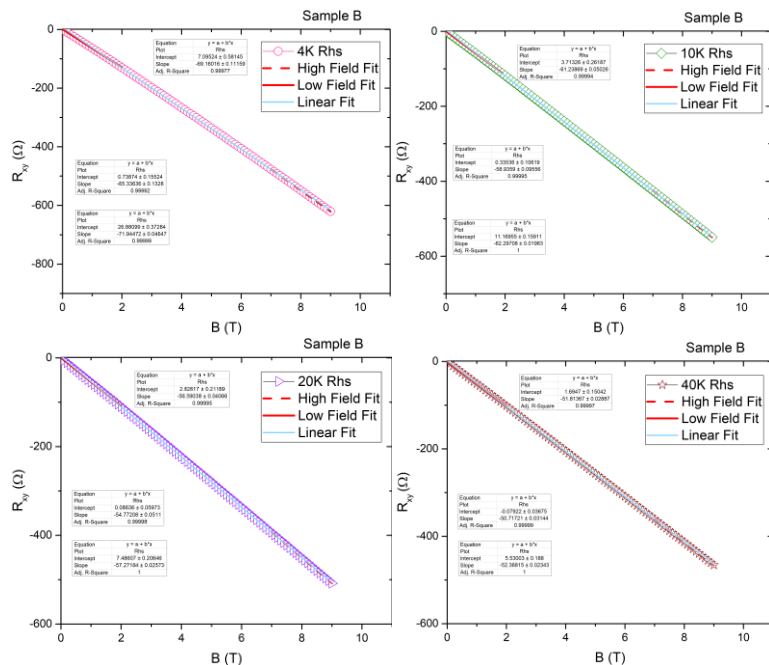


Figure 43. Hall slope. the R_{xy} slope and multiple range fits for 4K (top left) 10K (top right) 20K (bottom left) and 40K (bottom right).

temperature compared with the change in $(\delta\sigma_d)_{EEI}$ as a function of temperature follows the expected EEI theory. This shows that the reduction in carrier concentration with decreasing temperature is an effect of EEI and not a product of leakage current or other extrinsic effects. The R_{xy} of 2K

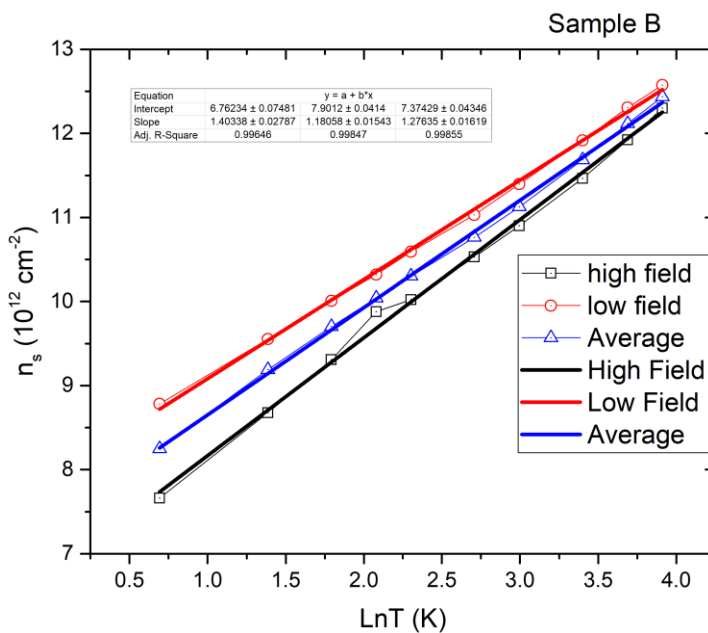


Figure 44. Carrier concentration vs $\ln T$. the high field, low field, and average carrier

different slopes were extracted from $T = 2$ K to $T = 40$ K and then plotted. In figure 43 the fitting of the multiple carries for $T = 4$ K, 10 K, 20 K, and 40 K are shown. The hall slopes in figure 42 are used to get the carrier concentration at high and at low fields. The slope of the (0-9T) range is

referred to as the average carrier concentration and in figure 44 the three different carrier concentrations are plotted with respect to temperature. The low field shows a higher carrier concentration than the high field. If the two carriers have significantly different mobilities, the asymptotic value of RH at zero field gives the density of the high mobility

Table 4. Sample carrier concentrations

Sample	Thickness (t)	K_{ee}	Diffusion constant (D)	$\frac{\sigma_D}{G_0}$	2 K n_s average	2 K n_s high field	2 K n_s low field	low – high field
160523-01	19.9 nm	.37	1.690E-4 m^2/s	14	1.753E13 cm^{-2}	1.655E13 cm^{-2}	1.831E13 cm^{-2}	1.76E12 cm^{-2}
161206-01	23.7 nm	.26	1.536E-4 m^2/s	10	8.24E12 cm^{-2}	7.659E12 cm^{-2}	8.78E12 cm^{-2}	1.121E12 cm^{-2}
161207-01	21.5 nm	.74	1.844E-4 m^2/s	11	1.818E13 cm^{-2}	1.804E13 cm^{-2}	1.95E13 cm^{-2}	1.46E12 cm^{-2}

carriers, $n_{hi} = \frac{1}{eR_0}$, whereas its value at large fields yields the total density of both

carriers, $n_{total} = \frac{1}{eR_\infty}$.⁹ In table 4 the different high and low field carrier concentrations are listed for the different samples. The carrier concentration does not follow the expected trend from the Lifshitz interpretation of multi band filling. In our data the low field concentration is larger than the high field concentration.

5.5 Parabolic HLN Fitting

The hall resistance measurement shows a slight non-linearity that may indicate the presence of a second type of charge carriers in the system. The 1-parameter and 2-parameter HLN fittings that were previously used did not consider the possibility of two carries.

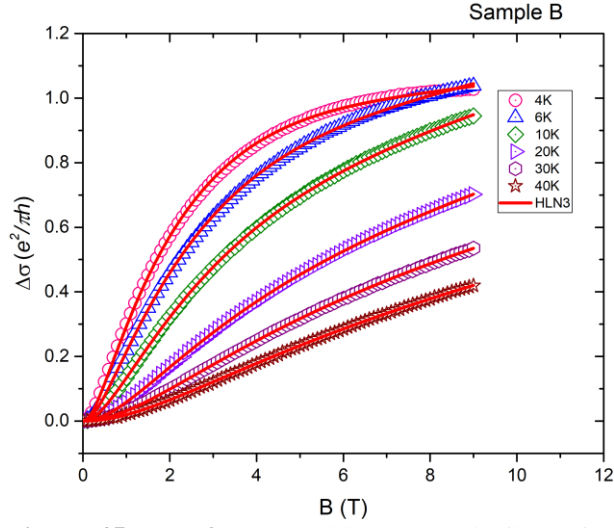


Figure 45. HLN3. The positive magnetic field of the MC. With a 3 parameter HLN fitting

$$MC = \left[\psi\left(\frac{1}{2} + \frac{B\phi}{B}\right) - \ln \frac{B\phi}{B} \right] - D \left[\frac{B^2}{1+(mB)^2} \right] [\text{HLN3}]$$

The new variation of the HLN equation has two new parameters for fitting D which is related to the second carrier, and m is related to the mobility seen in figure 45. The new fitting will now give the phase coherence field as well as the values for the second carrier. Unlike the previous 1 and 2 parameter HLN fittings, the HLN3 fitting can fit the full data range at 2 K as shown in figure 46. In figure 47 the fitting parameters, D, and m from the

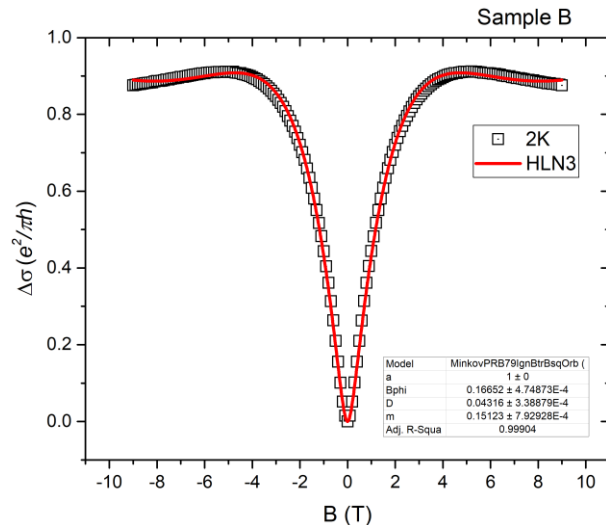


Figure 46: 2K MC HLN3. data at 2K with a 3 parameter HLN fitting that cover the full range

$T=2,4,6,8,10,15,20,30$, and 40 K HLN3

equation are plotted versus temperature. As expected, D and m both increase in magnitude as the temperature is decreased.

The HLN3 fitting is the first model that can fit the full data range at 2 K but the phase coherence field is the one parameter that is shared among all three fittings. Figure 48 has the phase coherence field from the different fitting plotted on the same scale and they are almost equal to one another. The HLN fitting results for the phase coherence field agree very well for all fittings.

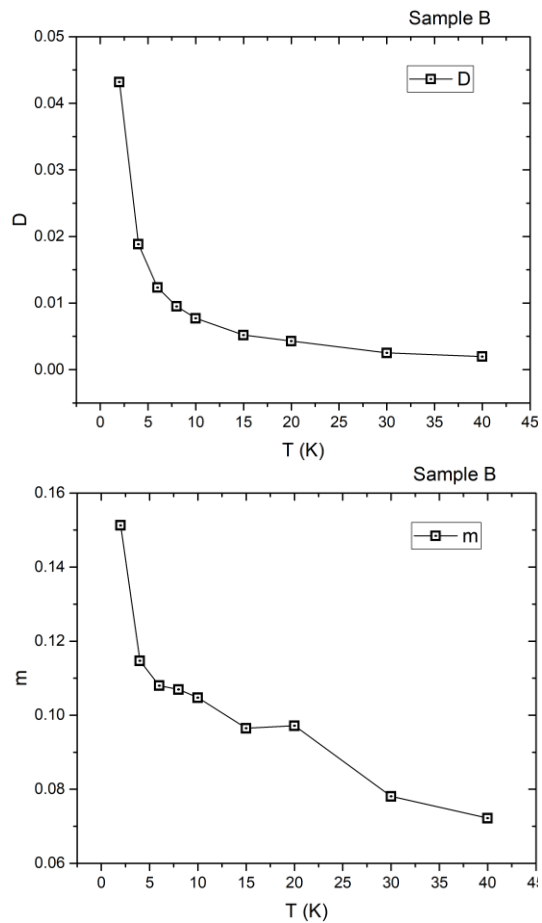


Figure 47. D HLN3. The second carrier fitting parameter from the HLN3 fitting.

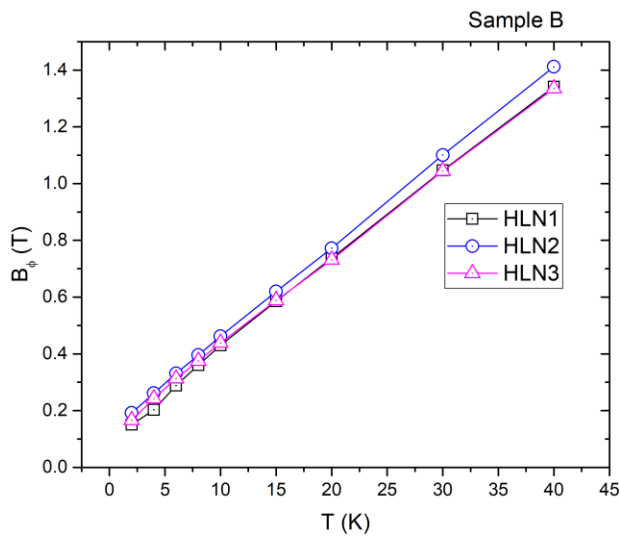


Figure 48. HLN 1,2,3. The phase coherence field from all three HLN fittings

6. CONCLUSIONS

6.1 Conclusions

The strained SrTiO₃ films epitaxially grown on p-Si (100) presented in this thesis work show an lnT dependence of the conductance and negative MR. hallmarks of 2D electron system.

The 2D electron system has a long phase coherence length and thermal length (l_t). In figure 49 (top) the phase coherence length l_ϕ is plotted as a function of temperature. It increases as the temperature increases and below 12 K the phase coherence length exceeds the sample thickness.

The low temperature l_ϕ is longer than the thickness which

justifies the 2D approach to the QCC analysis. In figure 48 (bottom) the l_t decreases with increasing temperature similarly to l_ϕ . At higher temperatures, we still observe negative MR and lnT dependence of the conductivity indicating that 2d behavior and confinement

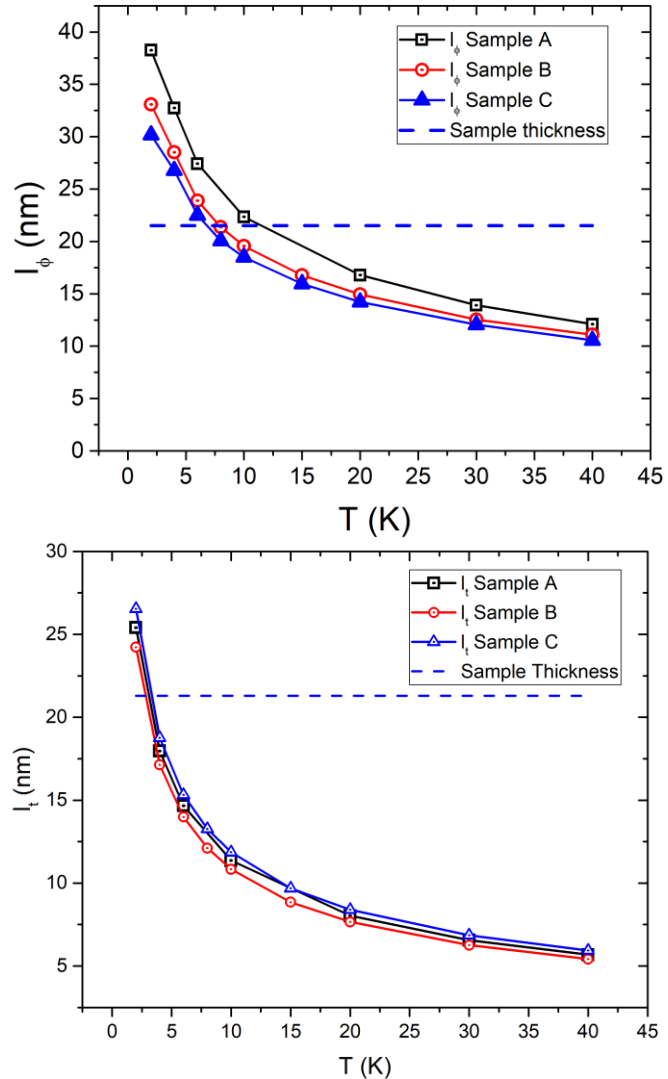


Figure 49. Characteristic Lengths. (top) Phase coherences length (bottom) Thermal length.

persist up to 30 K. At 30 K, $l_t \sim 6$ nm which sets the upper limit for the 2DES effective thickness. The 2DEG can be located either at the surface of SrTiO₃⁷ or near the interface due to the strain gradient. Nevertheless, the 6 nm confinement length is close the 2.5 nm

Table 5. Sample substrates					
Sample	Substrate	Substrate Resistivity $\Omega\cdot\text{cm}$	Resistance 300 K Ω	Mobility 300 K cm^2/Vs	Doping Boron 10^{15} cm^{-3}
160523-01 Sample A	p-Si(100)	5-10	180-360	407-414	3-1.5
161206-01 Sample B	p-Si(100)	1-5	36-180	370-407	16-3
161207-01 Sample C	p-Si(100)	0.1-0.5	4-18	235-334	250-40
161208-01 Sample D	p-Si(100)	5-10	180-360	407-414	3-1.5

critical thickness for strain relaxation for SrTiO₃ on Si(001)¹³. The non-linearity of the Hall slope is evidence of perhaps a second carrier. The estimated mobility for our films at 2 K is $\sim 50 \text{ cm}^2/\text{Vs}$ which is much lower than the mobility of p-Si at the doping levels indicated on Table 5. STO/LAO also shows multi band carrier filling because of the Lifshitz transition with a critical carrier concentration of $1.68 \times 10^{13} (\text{cm}^{-2})$.⁹ The carrier concentration can be tuned field gating. Above the critical carrier concentration, the low field Hall slope is higher and represents the high mobility carriers while at high fields the Hall slope is decreases and gives the total carrier concentration according to a simple two-carrier system behavior. Below the critical carrier concentration, this trend is reversed, and the low field Hall slope is smaller than the Hole slope at high fields. This is similar to the behavior that we are observing. Below the carrier concentration threshold, the difference between the high and low field sloped are small $\sim 10^{12} \text{ cm}^{-2}$. The samples used in this study have carrier concentrations that are right at this threshold ($< 2 \times 10^{13} \text{ cm}^{-2}$)

²⁾) and also show very small differences in carrier concentration for high and low magnetic fields $1\text{-}2 \cdot 10^{12} \text{ cm}^{-2}$. So our Hall measurements show similar evidence of multiple carriers which follow the expected theory of multi band carrier filling due to Lifshitz transition. Samples A, B, and C all show this behavior irrespective of the different doping level of the p-type Si substrate seen in table 5. It seems that the secondary carriers are not being contributed from the substrate. Even more, the similarity of the MC behavior, the almost identical values for the phase coherence and thermal lengths for all three samples indicate that the substrate doping doesn't affect the electronic properties

6.2 Hall bar data

Cr has a low oxide growth but a 2nm native oxide film is expected to be present and Cr (IV) oxide is ferromagnetic with a Curie temperature of 390K⁴² which can negatively impact magnetic measurements. The ratio of the size of the contacts compared to sample size is very small on a Van Der Pauw structure (~.001); however, with the 60-20 Hall ball, the contacts are approximately 1500 times larger in surface area than the sample. The magnetic properties of Cr oxide dose not significantly affect the Van Der Pauw measurements due to the small surface area size, but the larger contact size of the hall bar means that the Cr oxide dominates the magnetic measurements. In figure 20 preliminary data showed evidence that the Cr contacts contribute to the MR measurement of the Hall bars, so an alternative to Cr is needed.

Aluminum (Al) with a work function of 4.06 eV - 4.26 eV is the metal of choice for other STO systems⁴³. To help limit the formation of Al₂O₃, a thin (15nm) layer of gold (Au) is deposited on the top of the Al before the sample is exposed to the atmosphere. This cap layer of Au prevents Oxygen (O) in the atmosphere from oxidizing the surface of the Al.

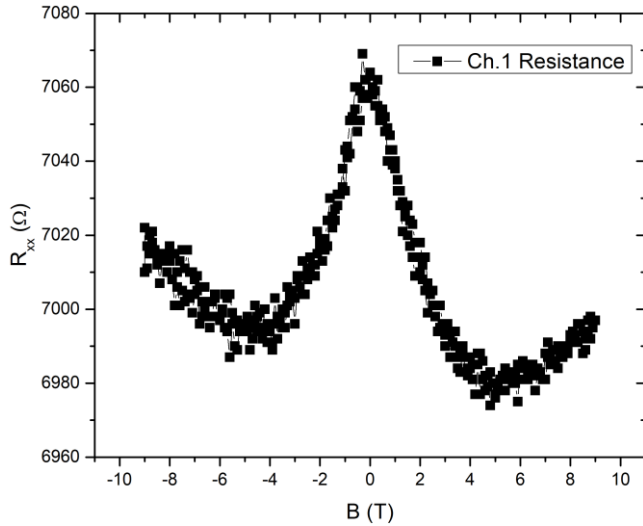


Figure 50: Cr contacts. on a STO Hall bar which negatively contribute to the MR measurement.

After processing several samples with Al contacts; electrical testing revealed that the resistance of the Hall bars did not correlate to the resistance of the Van Der Pauw samples. “Metals that have an oxide enthalpy of formation that is larger in magnitude than the oxygen vacancy formation energy of STO, which is commonly taken to be 6.0eV/vacancy, could potentially take oxygen from the STO surface region as well”⁴⁴. From this, we concluded that the Al contacts though protected from oxidation by the cap layer of Au are oxidizing from scavenged oxygen obtained from the STO film. “Oxidizable metals that have similar work function to STO such as Al create an oxygen-deficient STO layer⁴⁴”. The change in oxygen vacancies of the STO layer changes the resistance of the film as well as possibly the carrier concentration of the sample. In figure 21 (top) the R_{xy} slope of Cr and Ti-Au show a very strong correlation however the Al-Au contacts differ from the other two contacts. Figure 21 (bottom) shows

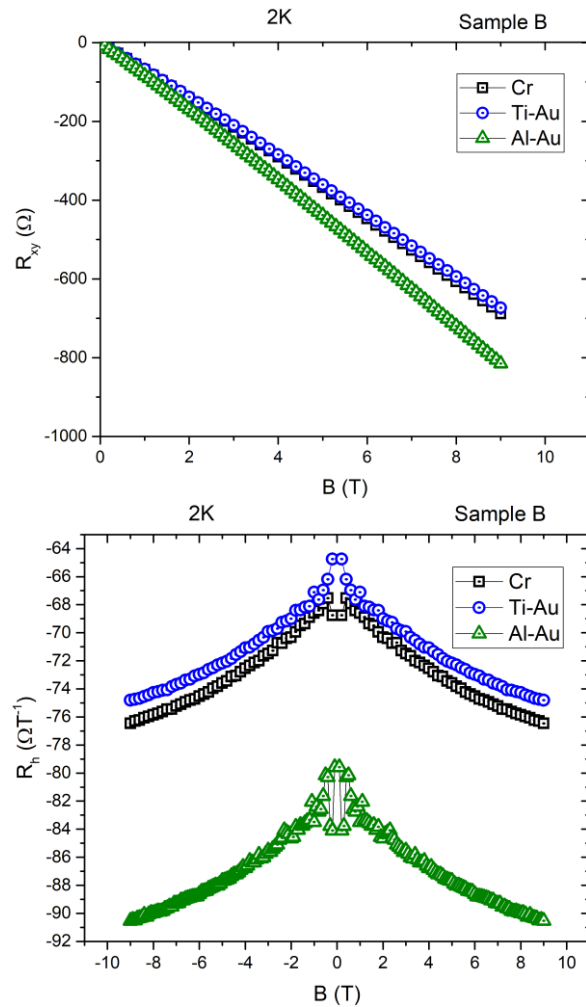


Figure 51. Different contacts. shows a comparison of three different contact materials. The R_{xy} slope (top) shows a significant difference of the Al contacts from the other two. The hall resistance (bottom) shows similar supporting evidence that the carrier concentration may

the plot of the hall vs magnetic field and there is a clear deviation of the Al-Au sample which may be a result of the contacts changing the carrier concentration. Another concern is intermetallic formation between Au/Al that is well studied in the semiconductor industry.⁴⁵ After becoming aware of the issues with Al/Au contacts, and given the fact that the Hall bar structures did not show scalable results, a different metal for the contacts was needed. Using previous work as a starting point “Electrical contacts are made to the LAO/STO interface by Ti/Au (2 nm /23 nm) sputter deposition⁴⁶”, the metallization process was modified to allow for the creation of 5/100 nm Ti/Au metal contacts. The previously used measurement was a DC setup and to attempt to overcome some challenges that this presented; the development of an AC setup was started. The previous

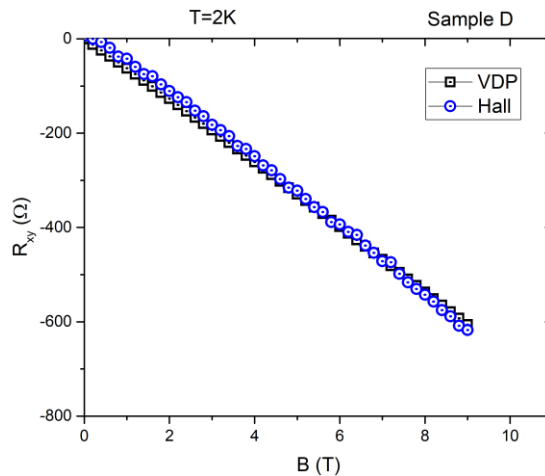


Figure 53: R_{xy} of AC. hall and Van der Pauw measurements plotted versus magnetic field

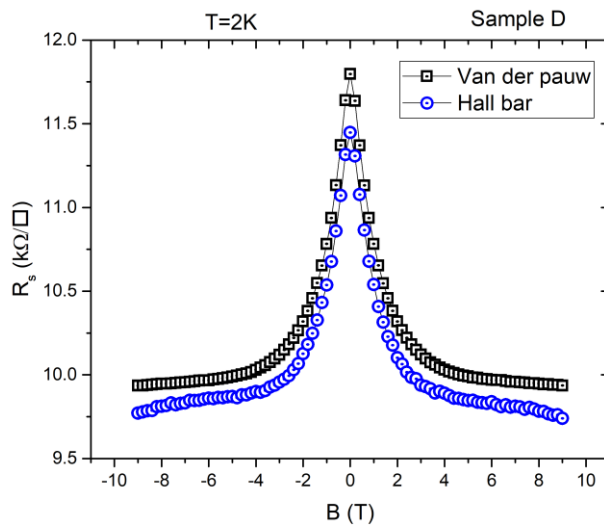


Figure 52: MR. of AC hall and Van der Pauw measurements plotted versus magnetic field

LabVIEW program was modified to work with a SR 830 lock-in amplifier and Keithley AC current source. The setup is still being tested for functionality but in figure 47 the preliminary data shows a strong correlation between the Van der Pauw

and Hall measurements. The MR data in figure 47 shows symmetric results that have a magnitude roughly equal to that obtained from the Van der Pauw technique. In figure 48, the R_{xy} for the two different measurements are compared and have a very close correlation. These are promising results after the changes faced using the DC measurement, but it is still too early to use this measurement in analyses of the system.

6.3 Future Directions

The analysis of the magnetotransport from the Van Der Pauw geometry shows the presence of a 2D system. The current Van der Pauw measurement uses a DC configuration which requires careful selection of currents to maintain a good signal to noise ratio. The development of an AC measurement configuration which can maintain a good signal to noise ratio with a much smaller current setting. The DC hall bar measurements show mixing of symmetric and asymmetric measurements along with a large noise level that requires high current to obtain data. The preliminary AC hall data show an improvement in noise that allows for measurements of voltages that are 3 orders of magnitude lower than the DC set up. The preliminary data also shows an ability to replicate Van der pauw data that was not previously seen. The AC configuration is in development but requires more adjustment. Preliminary magneto conductance and RvT data of the show the same data across the two different structures. The hall measurement shows unexpected deviations such as symmetric data bleeding into an asymmetric configuration. Advancing my research will require further development of the AC measurements system. After the AC technique is verified the inclusion of parallel field measurements will be added to the data collection. In the absence of spin-orbit scattering or magnetic impurities, orbital contributions to the MC are quenched in parallel fields and the negative MR due to WL should disappear.

APPENDIX SECTION

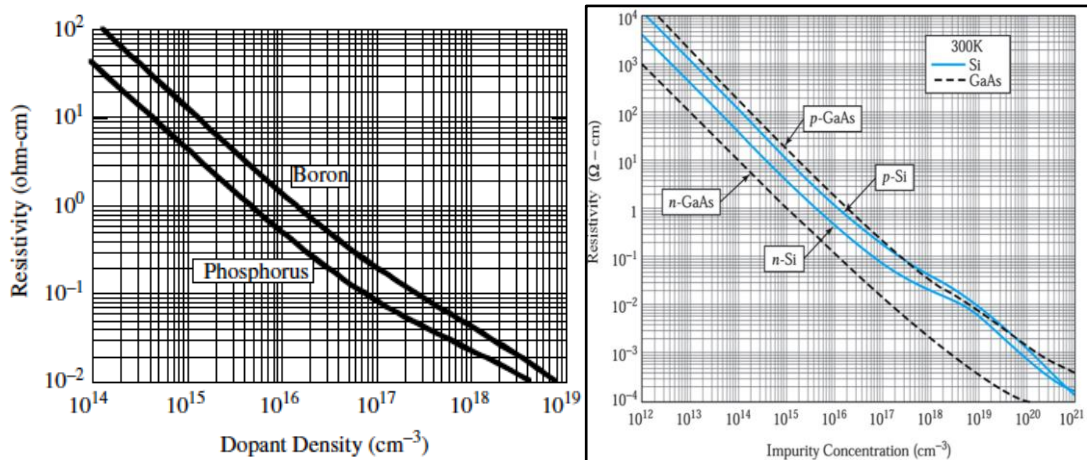


Figure 54: Resistivity vs Dopant density for Boron and Phosphorus doped Silicon at 300 K

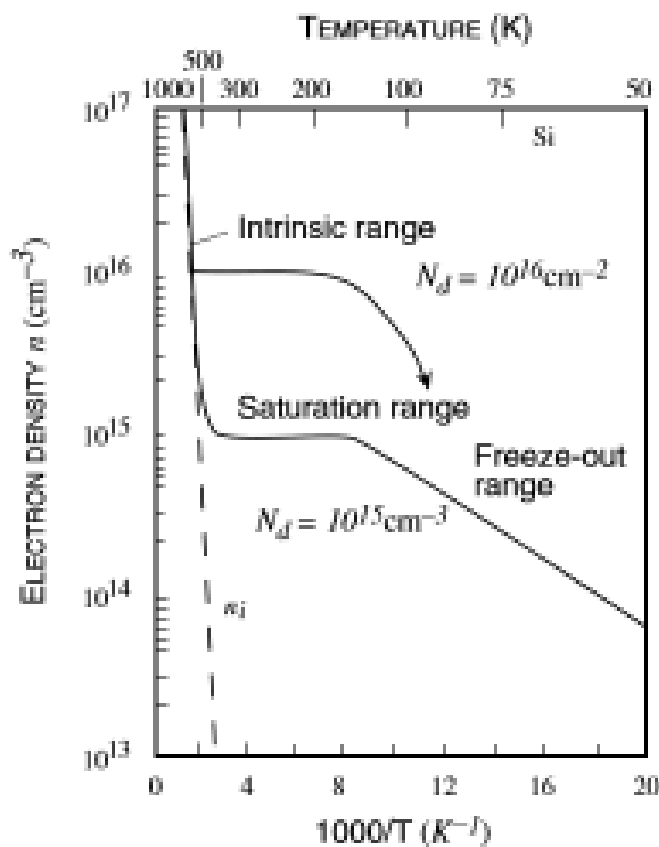


Figure 55.

The Si substrate at room temperature is in its Saturation range where the carrier concentration is a constant value which does not change with temperature. As the Si is cooled down further it enters the Freeze-out range were the carrier concentration decreases linearly with respect to inverse Kelvin. In the Freeze-out range there are no free carriers to contribute to measurements.

REFERENCES

1. S. Piskunov, E. Heifets, R. I. Eglitis and G. Borstel, Computational Materials Science **29** (2), 165-178 (2004).
2. A. Spinelli, M. A. Torija, C. Liu, C. Jan and C. Leighton, Physical Review B **81** (15) (2010).
3. A. Joshua, J. Ruhman, S. Pecker, E. Altman and S. Ilani, Proc. Natl. Acad. Sci. U. S. A. **110** (24), 9633-9638 (2013).
4. Y. Kozuka, M. Kim, H. Ohta, Y. Hikita, C. Bell and H. Y. Hwang, Applied Physics Letters **97** (22) (2010).
5. M. J. Han, C. A. Marianetti and A. J. Millis, Physical Review B **82** (13) (2010).
6. N. Nakagawa, H. Y. Hwang and D. A. Muller, Nature Materials **5** (3), 204-209 (2006).
7. A. F. Santander-Syro, O. Copie, T. Kondo, F. Fortuna, S. Pailhes, R. Weht, X. G. Qiu, F. Bertran, A. Nicolaou, A. Taleb-Ibrahimi, P. Le Fevre, G. Herranz, M. Bibes, N. Reyren, Y. Apertet, P. Lecoeur, A. Barthelemy and M. J. Rozenberg, Nature **469** (7329), 189-193 (2011).
8. A. Ohtomo and H. Y. Hwang, Nature **427** (6973), 423-426 (2004).
9. A. Joshua, S. Pecker, J. Ruhman, E. Altman and S. Ilani, Nature Communications **3** (2012).
10. H. Mori and H. Ishiwara, Japanese Journal of Applied Physics Part 2-Letters **30** (8A), L1415-L1417 (1991).
11. R. J. Cottier, N. A. Steinle, D. A. Currie and N. Theodoropoulou, Applied Physics Letters **107** (22) (2015).
12. F. S. Aguirre-Tostado, A. Herrera-Gomez, J. C. Woicik, R. Droopad, Z. Yu, D. G. Schlom, P. Zschack, E. Karapetrova, P. Pianetta and C. S. Hellberg, Physical Review B **70** (20) (2004).
13. M. P. Warusawithana, C. Cen, C. R. Sleasman, J. C. Woicik, Y. Li, L. F. Kourkoutis, J. A. Klug, H. Li, P. Ryan, L.-P. Wang, M. Bedzyk, D. A. Muller, L.-Q. Chen, J. Levy and D. G. Schlom, Science **324** (5925), 367-370 (2009).
14. J. Robertson, J. Vac. Sci. Technol. B **18** (3), 1785-1791 (2000).
15. S. A. Chambers, T. Droubay, T. C. Kaspar and M. Gutowski, Journal of Vacuum Science & Technology B **22** (4), 2205-2215 (2004).
16. S. A. Chambers, Y. Liang, Z. Yu, R. Droopad and J. Ramdani, Journal of Vacuum Science & Technology a-Vacuum Surfaces and Films **19** (3), 934-939 (2001).
17. S. A. Chambers, Y. Liang, Z. Yu, R. Droopad, J. Ramdani and K. Eisenbeiser, Applied

- Physics Letters **77** (11), 1662-1664 (2000).
18. F. Amy, A. S. Wan, A. Kahn, F. J. Walker and R. A. McKee, Journal of Applied Physics **96** (3), 1635-1639 (2004).
 19. J. C. Woicik, E. L. Shirley, C. S. Hellberg, K. E. Andersen, S. Sambasivan, D. A. Fischer, B. D. Chapman, E. A. Stern, P. Ryan, D. L. Ederer and H. Li, Physical Review B **75** (14) (2007).
 20. J. Gazquez, M. Stengel, R. Mishra, M. Scigaj, M. Varela, M. A. Roldan, J. Fontcuberta, F. Sanchez and G. Herranz, Physical Review Letters **119** (10) (2017).
 21. Y. Matsubara, K. S. Takahashi, M. S. Bahramy, Y. Kozuka, D. Maryenko, J. Falson, A. Tsukazaki, Y. Tokura and M. Kawasaki, Nature Communications **7** (2016).
 22. R. E. Hummel, *Electronic Properties of Materials*, 4 ed. (Springer, 2010).
 23. T. Ando, A. B. Fowler and F. Stern, Rev. Mod. Phys. **54** (2), 437-672 (1982).
 24. B. L. Altshuler and A. G. Aronov, *Electron-electron interactions in disordered systems*. (Elsevier, 1985).
 25. A. P. Dmitriev, V. Y. Kachorovskii and I. V. Gornyi, Physical Review B **56** (15), 9910-9917 (1997).
 26. S. J. Allen, B. Jalan, S. Lee, D. G. Ouellette, G. Khalsa, J. Jaroszynski, S. Stemmer and A. H. MacDonald, Physical Review B **88** (4) (2013).
 27. G. M. Minkov, A. V. Germanenko, O. E. Rut, A. A. Sherstobitov and B. N. Zvonkov, *Antilocalization in gated 2D quantum well structures with composition gradient*. (2003).
 28. S. Hikami, A. I. Larkin and Y. Nagaoka, Prog. Theor. Phys. **63** (2), 707-710 (1980).
 29. I. L. Aleiner, B. L. Altshuler and M. E. Gershenson, Waves Random Media **9** (2), 201-239 (1999).
 30. B. N. Narozhny, G. Zala and I. L. Aleiner, Physical Review B **65** (18), 4 (2002).
 31. B. L. Altshuler, D. Khmelnitzkii, A. I. Larkin and P. A. Lee, Physical Review B **22** (11), 5142-5153 (1980).
 32. G. M. Minkov, A. V. Germanenko, O. E. Rut, A. A. Sherstobitov and B. N. Zvonkov, Physical Review B **75** (23) (2007).
 33. G. M. Minkov, O. E. Rut, A. V. Germanenko, A. A. Sherstobitov, V. I. Shashkin, O. I. Khrykin and B. N. Zvonkov, Physical Review B **67** (20) (2003).
 34. G. M. Minkov, O. E. Rut, A. V. Germanenko, A. A. Sherstobitov, B. N. Zvonkov, E. A. Uskova and A. A. Birukov, Physical Review B **65** (23) (2002).
 35. I. Shlimak, Is Hopping a Science? : Selected Topics of Hopping Conductivity, 1-139

(2015).

36. S. M. Sze and K. K. Ng, *Physics of Semiconductor Devices*, 3 ed. (Wiley-Interscience, 2007).
37. K. Instruments, (no, 2012).
38. D. W. Koon, Review of Scientific Instruments **60** (2), 271-274 (1989).
39. H. Li, X. Hu, Y. Wei, Z. Yu, X. Zhang, R. Droopad, A. A. Demkov, J. Edwards, K. Moore, W. Ooms, J. Kulik and P. Fejes, Journal of Applied Physics **93** (8), 4521-4525 (2003).
40. J. R. a. C. W. Chen, APPLIED PHYSICS LETTERS **74** (1999).
41. C. Capan, G. Y. Sun, M. E. Bowden and S. A. Chambers, Applied Physics Letters **100** (5), 052106 (2012).
42. G. P. Singh and S. Ram, Journal of Magnetism and Magnetic Materials **322** (9-12), 1484-1487 (2010).
43. P. M. Clayton A. Jackson, S. James Allen, and Susanne Stemmer, APPLIED PHYSICS LETTERS (2012).
44. K. J. K. Agham B. Posadas, Wei Guo, Patrick Ponath, Jacqueline Geler-Kremer, Tobias Hadamek, and Alexander A. Demkova, JOURNAL OF APPLIED PHYSICS (2017).
45. G. K. C. Chen, Ieee Transactions on Parts Materials and Packaging **PMP3** (4), 149-& (1967).
46. J. P. V. Guanglei Cheng, Patrick Irvin, Cheng Cen,, Daniela F. Bogorin,, Feng Bi, Mengchen Huang, Shicheng Lu, Chung-Wung Bark, Sangwoo Ryu, Kwang-Hwan Cho, Chang-Beom Eom, and Jeremy Levy, PHYSICAL REVIEW X **3** (2013).